Banner appropriate to article type will appear here in typeset article

Three-dimensional curved detonation equations

Hao Yan[1], Chongguang Shi[1], Ralf Deiterding[2], Haochen Xiong[1], Xin Han[1], and Yancheng You[1] †

[1]School of Aerospace Engineering, Xiamen University, Xiamen, Fujian 361005, PR China
[2]School of Engineering, University of Southampton, Southampton, SO16 7QF, UK

(Received xx; revised xx; accepted xx)

This paper describes the derivation and development of three-dimensional curved detonation equations and presents analysis and applications. Gradient equations are established for both the pre- and post-wave phenomena associated with three-dimensional curved detonation. These equations delineate a gradient relationship, enabling the resolution of multiple aerodynamic gradient parameters within the context of the three-dimensional detonation wave. The equations can be used to analyse the influence coefficients regarding post-wave gradients, allowing both the pattern and magnitude of each affected gradient to be determined. Calculations and analysis of the gradients trailing the curved detonation surface clarify the variation in gradients along the geometric boundary. The accuracy of the proposed theory is verified through comparisons with simulation results. By integrating zero-order parameters with first-order gradients, the evolving patterns of three-dimensional post-wave parameters are effectively distinguished. Moreover, the theory facilitates an examination of the effects of incoming flow parameters and energy release on post-wave gradients. Further investigations into detonation waves of varying curvatures reveal the influence of the curvature on the gradient characteristics. A method for solving the wave function based on waveform gradients is devised, enabling precise calculations of the corresponding detonation wave shape. Comparative analysis with experimental results demonstrates the efficacy of the inverse solving approach. In summary, three-dimensional curved detonation theory represents a significant advance in detonation studies, transitioning from two- to three-dimensional analysis. This shift elevates the research paradigm from zero-order parameters to first-order gradients, leading to a more comprehensive and nuanced comprehension of the aerodynamics inherent in three-dimensional detonation.

1. Introduction

Detonation is an extreme shock-wave-induced combustion phenomenon that has garnered widespread attention owing to its self-sustaining propagation, supersonic flame, and high thermodynamic efficiency (Wolański 2013). Detonation studies have covered one-, two-, and three-dimensional analyses. One-dimensional (1D) detonation was frequently considered in early detonation studies, and is presently used to calculate variations in fundamental parameters such as velocity and pressure. However, 1D studies have a limited research

---

† Email address for correspondence: yancheng.you@xmu.edu.cn

Abstract must not spill onto p.2

scope and are unable to fully capture the structural characteristics of detonation. Two-dimensional (2D) representations are the prevailing configuration in current research, capable of reflecting numerous important aspects such as the structural characteristics and parameter distribution of detonation. Although three-dimensional (3D) spatial studies provide a more comprehensive description of detonation wave structures than 2D representations, their numerical simulations demand substantial computational resources, resulting in limited comprehension of the mechanisms and characteristics of 3D detonation. Research using 1D, 2D, and 3D configurations reveals unique and complementary characteristics, thereby enhancing the study of detonation.

Studies on 1D detonation have predominantly concentrated on the investigation of positive detonation phenomena. Theoretical analyses typically employ the Chapman–Jouguet (CJ) theory to determine the minimum propagation speed of the detonation wave, in accordance with conservation laws (Viguier *et al.* 1996). This velocity consistently aligns with experimental findings. The Zel'dovich–von Neumann–Doering (ZND) model describes a detonation structure consisting of an induced shock surface and a reaction zone, which provides the ignition and driving mechanism of the detonation wave (Zel'dovich 1940; von Neumann 1942; Doering 1943). Agafonov & Frolov (1994) established a theoretical solution model for 1D detonation in hydrogen mixtures, which has consistently demonstrated strong agreement with experimental data regarding the reaction zone length and detonation diameter. Employing the 1D Euler equation for finite-rate chemical reactions, they investigated the structure and stability of ethylene–air mixtures, and by varying the equivalence ratio, pressure, and overdrive ratio, derived an unsteady oscillating model of the detonation wave (Yungster *et al.* 2003). He & Lee (1995) investigated the influence of variations in activation energy on the dynamics of detonation propagation using numerical simulations. Two critical activation energies were found to correspond to three states: stability, galloping oscillations, and an inability to self-sustain propagation.

The study of 2D detonation has received significant attention. Teng *et al.* (2021) undertook numerical and theoretical investigations into the morphology of oblique detonation waves (ODWs) in hydrogen gas. They analysed two distinct detonation wave scenarios. One suggests that a compression wave could instigate alterations, while the other scenario proposes that the classical secondary ODW might transition into a normal detonation wave. Based on these phenomena, four different ODW systems were delineated and discussed. Choi *et al.* (2007) explored the influence of grid resolution and activation energy on cell structure through numerical simulations. Their findings revealed that the detonation front can maintain stability at low activation energies, but becomes unstable and manifests significant changes in cell structure under high-activation-energy conditions. In a separate investigation, Liu *et al.* (2016) investigated ODWs induced by finite wedges using numerical simulation methods. The results demonstrated that initiating combustion in the initial flow field in advance led to a reduction in induced length. Teng & Jiang (2012) investigated smooth and abrupt detonation wave morphogenesis and its dependence on the incoming flow conditions, reactant properties, and energy release rates. A criterion for judging the form of the transition was developed in terms of the difference between the detonation angle and the shock angle. Simulation results demonstrated the accuracy of this criterion. Jiang *et al.* (2021) conducted experiments on oblique detonation engines and successfully achieved both strong detonation and oblique detonation combustion modes by adjusting the geometric structure of the combustion chamber. These findings provided empirical validation for the feasibility of oblique detonation engines.

In the realm of 2D axisymmetric detonation, Yang *et al.* (2017) used a one-step irreversible Arrhenius reaction kinetic model to conduct numerical investigations into the ODW structures induced by semi-infinite cones. Simulations revealed the interaction between circumferential curvature and energy release, and a novel oblique detonation initiation structure was discovered. Verreault & Higgins (2011) investigated the initiation of detonation in conical projectiles and proposed energy and kinetic limits to predict the conditions required in mixed gases. The data indicate that the detonation limits derived from both theories are in accord with experimental outcomes. Experiments also captured five combustion regimes, including rapid and delayed ODW formation, combustion instability, wave splitting, and inert shock waves. Lefebvre & Fujiwara (1995) scrutinized the overall shape of ODWs supported by conical bodies, outlining four typical combustion modes. When the tip radius is small, the coupling between the shock wave and the reaction zone occurs at a higher Mach number. When the tip radius is large, the transition from deflagration to detonation will not be as smooth as when the radius is small.

Although there have been relatively few studies on 3D detonation, the structural characteristics and variation rules of detonation waves in three dimensions have been revealed. Han *et al.* (2019) employed a 3D numerical simulation of conical detonation waves, and found that an increase in heat release leads to a transformation of the detonation waves from smooth to abrupt forms. In addition, the wave surfaces change from being smooth to exhibiting cellular features. Comparatively weaker than planar 2D ODWs, those induced by conical bodies exhibit prolonged structures. Moreover, cones moderate and delay the transition from oblique shock waves to ODWs compared with wedges. Crane *et al.* (2023) conducted 3D simulations of detonation in square and circular tube geometries and compared the results with 2D experiments, emphasizing the impact of constraints and boundaries on the detonation structure. The results indicate that the intersection of transverse waves in 3D detonation can lead to extreme thermodynamic conditions and highly overdriven wave velocities, far exceeding those predicted by the ZND model and 2D simulations. While the square channel yields a regular structure with shock waves forming a square lattice, the circular tube channel produces more complex and dispersed detonations. Additionally, Gato (2010) investigated 3D aluminium detonation, revealing that only a small fraction of the detonation wave energy is converted to gas and particle lateral kinetic energy, illustrating the consistency of the 3D detonation propagation speed with the ideal CJ value. Furthermore, Wang *et al.* (2008) developed a 3D detonation solver to explore spinning 3D detonation. The simulation results highlight the detonation instability, overdrive, lateral size, and initial disturbance as pivotal factors influencing the occurrence of spinning detonation waves. In terms of experiments, Maeda *et al.* (2013) discussed the impact of the curvature effect on the detonation stability arising from the 3D nature of the projectile. These experimental findings reveal that increased curvature diminishes the velocity of the detonation wave near the projectile to a lower level than the CJ velocity. Research by Kaneshige & Shepherd (2002) demonstrated that, as the projectile velocity approaches the CJ velocity of detonation, the detonation wave undergoes a prolonged initiation and settling period, eventually stabilizing into a steady waveform. Moreover, an elevated experimental pressure leads to an overdriven detonation, which resembles positive detonation.

The progress of the abovementioned research highlights the urgent need for studies on detonation in 3D space. In contrast to numerical simulations, theoretical research is notably deficient. This paper first derives the 3D curved detonation equations in gradient form within the vector space framework, drawing upon the Euler equations and single-step chemical reactions. Subsequently, the influence coefficients of the post-wave gradients are analysed, elucidating the patterns of variation for each gradient. Moreover, the impact of parameters such as the energy release and curvature on the post-wave gradient is further scrutinized. Finally, validation and inverse solution methods are presented to demonstrate the effectiveness and superiority of the equations derived in this study.

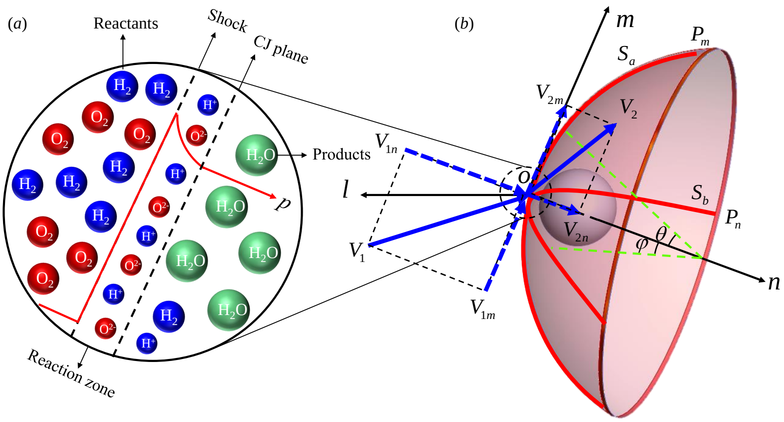

Figure 1: Schematic diagram of the 3D curved detonation wave: (*a*) chemical reaction process in detonation (take hydrogen for example), (*b*) geometry of the 3D wave.

2. Theoretical derivation of 3D curved detonation equations

2.1. *Theoretical assumptions and geometric model*

Before advancing with the theoretical derivations, it is vital to delineate two fundamental assumptions. The first posits that the detonation waves encountered in this article can be comprehended as waves, indicating that the shock waves and the chemical reactions are tightly coupled. The second assumption asserts that the chemical reactions within detonation adhere to the single-step Arrhenius equation. Once these assumptions are clarified, a 3D curved detonation wave model is considered, as depicted in figure 1. In the vector coordinate system (l, m, n), where the detonation wave is a continuous and smooth 3D surface, a unique tangent plane P_n exists at point O. The normal line of the tangent plane at O is denoted as n. The incoming flow velocity V_1 is decomposed into two components, V_{1m} and V_{1n}, along and perpendicular to the wave, respectively. V_2 is the post-wave velocity, and applying the same decomposition law gives V_{2m} and V_{2n}. The direction perpendicular to both the m- and n-directions is defined as the l-direction. The unit vectors in the three directions are $\overrightarrow{e_l}$, $\overrightarrow{e_m}$, $\overrightarrow{e_n}$, respectively. The planar curvature S_a is defined as the curvature along the m-direction, where the wave angle θ is the angle between the incoming flow velocity vector and the tangent surface P_m of the wave. The transversal curvature S_b is defined as the curvature along the n-direction, where φ is the angle between the incoming flow velocity vector and the tangent surface P_l of the wave. According to the geometric relationship, the velocity can be decomposed as follows:

$$\overrightarrow{V} = V_l\overrightarrow{e_l} + V_m\overrightarrow{e_m} + V_n\overrightarrow{e_n}, \tag{2.1}$$

where $\overrightarrow{V}$ is the velocity vector, V_l, V_m, V_n are the velocity components along the three directions, and e_l, e_m, e_n are unit vectors. Therefore, to solve for the gradient of velocity, we need to first solve for the gradients of the unit vectors along the three directions. The results are shown in equation (2.2); the specific derivation is given in Appendix A:

$$\begin{gathered}
\frac{\partial \overrightarrow{e_l}}{\partial l}=\frac{\partial \overrightarrow{e_l}}{\partial \varphi}\frac{\partial \varphi}{\partial l}=-\overrightarrow{e_n}S_b,\ \frac{\partial \overrightarrow{e_m}}{\partial l}=0,\ \frac{\partial \overrightarrow{e_n}}{\partial l}=\frac{\partial \overrightarrow{e_n}}{\partial \varphi}\frac{\partial \varphi}{\partial l}=\overrightarrow{e_l}S_b,\\
\frac{\partial \overrightarrow{e_m}}{\partial m}=\frac{\partial \overrightarrow{e_m}}{\partial \theta}\frac{\partial \theta}{\partial m}=-\overrightarrow{e_n}S_a,\ \frac{\partial \overrightarrow{e_l}}{\partial m}=0,\ \frac{\partial \overrightarrow{e_n}}{\partial m}=\frac{\partial \overrightarrow{e_n}}{\partial \theta}\frac{\partial \theta}{\partial m}=\overrightarrow{e_m}S_a,\\
\frac{\partial \overrightarrow{e_l}}{\partial n}=0,\ \frac{\partial \overrightarrow{e_m}}{\partial n}=0,\ \frac{\partial \overrightarrow{e_n}}{\partial n}=0.
\end{gathered} \tag{2.2}$$

The two curvatures of the detonation wave are defined according to their geometric relationship:

$$S_a=\frac{\partial \theta}{\partial m}, S_b=\frac{\partial \phi}{\partial l}. \tag{2.3}$$

2.2. *Euler equations in vector coordinate system*

Generally, the pre-wave flow is unreacted gas without energy release. However, the post-wave flow may have energy release due to remaining chemical reactions. To simplify the derivation, we uniformly adopt the Euler equation form with energy release. Thus, the pre-wave state can be achieved by setting the energy release to zero. The expression of the mass conservation term in the Euler equation is:

$$\nabla(\rho \overrightarrow{V})=0, \tag{2.4}$$

where ρ is the density. According to equation (2.1), its decomposition along the spatial vector coordinate system (l, m, n) can be obtained as:

$$\nabla[\rho(V_l\overrightarrow{e_l}+V_m\overrightarrow{e_m}+V_n\overrightarrow{e_n})]=0. \tag{2.5}$$

Further decomposition yields:

$$\overrightarrow{e_l}\frac{\partial(\rho V_l\overrightarrow{e_l}+\rho V_m\overrightarrow{e_m}+\rho V_n\overrightarrow{e_n})}{\partial l}+\overrightarrow{e_m}\frac{\partial(\rho V_l\overrightarrow{e_l}+\rho V_m\overrightarrow{e_m}+\rho V_n\overrightarrow{e_n})}{\partial m}+\overrightarrow{e_n}\frac{\partial(\rho V_l\overrightarrow{e_l}+\rho V_m\overrightarrow{e_m}+\rho V_n\overrightarrow{e_n})}{\partial n}=0. \tag{2.6}$$

The above equation can be simplified according to equation (2.2):

$$\frac{\partial \rho}{\partial m}V_m+\rho\frac{\partial V_m}{\partial m}+\frac{\partial \rho}{\partial n}V_n+\rho\frac{\partial V_n}{\partial n}+\rho V_n S_a+\rho V_n S_b=0, \tag{2.7}$$

where the detailed calculation is presented in Appendix B. Similarly, the momentum conservation equation (2.8) in the Euler equations can be converted into the form of equation (2.9):

$$\rho(\overrightarrow{V}\nabla)\overrightarrow{V}+\nabla p=0, \tag{2.8}$$

$$\begin{gathered}
\rho V_n\frac{\partial V_l}{\partial n}+\frac{\partial p}{\partial l}=0,\\
\rho V_m\frac{\partial V_m}{\partial m}+\rho V_n\frac{\partial V_m}{\partial n}+\frac{\partial p}{\partial m}+\rho V_m V_n S_a=0,\\
\rho V_m\frac{\partial V_n}{\partial m}+\rho V_n\frac{\partial V_n}{\partial n}+\frac{\partial p}{\partial n}-\rho V_m^2 S_a=0.
\end{gathered} \tag{2.9}$$

where p is the pressure. Before simplifying the energy conservation equation, it is necessary to introduce the single-step Arrhenius formula. The single-step chemical reaction based on the Arrhenius formula (Verreault 2012) is:

$$\sigma=-\rho k Z\exp(-Ea/RT), \tag{2.10}$$

where σ denotes the rate of chemical generation, k is the pre-factor, Ea denotes the activation energy, and Z is the chemical reaction process. Therefore, the chemical reaction does not occur in the pre-wave ($Z = 1$) state, but occurs fully in the CJ state ($Z = 0$). If the energy fully released by detonation is Q_0, then the energy release from chemical reaction process Q_d is:

$$Q_d = (1 - \mathrm{Z})Q_0. \tag{2.11}$$

Therefore, the energy release Q_c in the post-wave Euler equations is assumed to be ZQ_0. Under this assumption, the post-wave energy conservation equation can be simplified to:

$$\begin{gathered}\frac{\partial h}{\partial l} + V_m\frac{\partial V_m}{\partial l} + V_n\frac{\partial V_n}{\partial l} + \frac{\partial Q_c}{\partial l} = 0,\\ \frac{\partial h}{\partial m} + V_m\frac{\partial V_m}{\partial m} + V_n\frac{\partial V_n}{\partial m} + \frac{\partial Q_c}{\partial m} = 0.\end{gathered} \tag{2.12}$$

The specific enthalpy expression is:

$$\frac{\partial h}{\partial l} = \frac{\gamma R}{\gamma - 1}\frac{\partial T}{\partial l}, \frac{\partial h}{\partial m} = \frac{\gamma R}{\gamma - 1}\frac{\partial T}{\partial m}. \tag{2.13}$$

This gives the Euler equations in the form of the space vector coordinate system.

2.3. *Derivation of pre- and post-wave relationships*

When conceptualizing a detonation wave in the form of a wave, both its pre- and post-wave states adhere to the principles of mass and momentum conservation, equivalent tangential velocities, and are governed by the Arrhenius formula, as depicted in the following equation:

$$\begin{gathered}\rho_1 V_{1n} = \rho_2 V_{2n},\\ p_1 + \rho_1 V_{1n}^2 = p_2 + \rho_2 V_{2n}^2,\\ V_{1m} = V_{2m},\\ \rho_1 V_{1n} Z_1 - \rho_1 k Z_1 \exp(-\frac{Ea}{R_1 T_1}) = \rho_2 V_{2n} Z_2 - \rho_2 k Z_2 \exp(-\frac{Ea}{R_2 T_2}).\end{gathered} \tag{2.14}$$

The detailed derivation and solution of the above equations can be found in our previous study(Yan *et al.* 2024). In equation (2.14), there are four equations and five unknowns, thus necessitating a reduction in the number of unknowns. The gas assumption is adopted here:

$$p = \rho R T. \tag{2.15}$$

Thus, the density can be expressed as a function of pressure and temperature. According to equation (2.13), we find that:

$$\frac{\partial T}{\partial l} = \frac{\partial h}{\partial l}\frac{\gamma - 1}{\gamma R}, \frac{\partial T}{\partial m} = \frac{\partial h}{\partial m}\frac{\gamma - 1}{\gamma R}, \tag{2.16}$$

where the expression for the specific enthalpy can be written using equation (2.12) as:

$$\begin{gathered}\frac{\partial h}{\partial l} = -V_m\frac{\partial V_m}{\partial l} - V_n\frac{\partial V_n}{\partial l} - \frac{\partial Q_c}{\partial l}\\ \frac{\partial h}{\partial m} = -V_m\frac{\partial V_m}{\partial m} - V_n\frac{\partial V_n}{\partial m} - \frac{\partial Q_c}{\partial m}.\end{gathered} \tag{2.17}$$

Thus, the partial derivatives of the density along the three directions can be acquired as:

$$\begin{aligned}\frac{\partial\rho}{\partial l} &= \frac{1}{RT}\frac{\partial p}{\partial l} + \frac{\rho(\gamma-1)}{T\gamma R}V_m\frac{\partial V_m}{\partial l} + \frac{\rho(\gamma-1)}{T\gamma R}V_n\frac{\partial V_n}{\partial l} + \frac{\rho(\gamma-1)}{T\gamma R}\frac{\partial Q_c}{\partial l},\\ \frac{\partial\rho}{\partial m} &= \frac{1}{RT}\frac{\partial p}{\partial m} + \frac{\rho(\gamma-1)}{T\gamma R}V_m\frac{\partial V_m}{\partial m} + \frac{\rho(\gamma-1)}{T\gamma R}V_n\frac{\partial V_n}{\partial m} + \frac{\rho(\gamma-1)}{T\gamma R}\frac{\partial Q_c}{\partial m}.\end{aligned} \tag{2.18}$$

Replacing the density with pressure, velocity, and chemical reaction processes, and solving for the partial derivatives of equation (2.14) along both the l and m directions beginning with the conservation of mass, the following two equations can be obtained:

$$\begin{aligned}&V_{1n}(\frac{1}{RT_1}\frac{\partial p_1}{\partial l} + \frac{\rho_1(\gamma_1-1)}{T_1\gamma_1 R}V_{1m}\frac{\partial V_{1m}}{\partial l} + \frac{\rho_1(\gamma_1-1)}{T_1\gamma_1 R}V_{1n}\frac{\partial V_{1n}}{\partial l} + \frac{\rho(\gamma-1)}{T\gamma R}\frac{\partial Q_{c1}}{\partial l}) + \rho_1\frac{\partial V_{1n}}{\partial l} =\\ &V_{2n}(\frac{1}{RT_2}\frac{\partial p_2}{\partial l} + \frac{\rho_2(\gamma_2-1)}{T_2\gamma_2 R}V_{2m}\frac{\partial V_{2m}}{\partial l} + \frac{\rho_2(\gamma_2-1)}{T_2\gamma_2 R}V_{2n}\frac{\partial V_{2n}}{\partial l} + \frac{\rho(\gamma-1)}{T\gamma R}\frac{\partial Q_{c2}}{\partial l}) + \rho_2\frac{\partial V_{2n}}{\partial l},\\ &V_{1n}(\frac{1}{RT_1}\frac{\partial p_1}{\partial m} + \frac{\rho_1(\gamma_1-1)}{T_1\gamma_1 R}V_{1m}\frac{\partial V_{1m}}{\partial m} + \frac{\rho_1(\gamma_1-1)}{T_1\gamma_1 R}V_{1n}\frac{\partial V_{1n}}{\partial m} + \frac{\rho(\gamma-1)}{T\gamma R}\frac{\partial Q_{c1}}{\partial m}) + \rho_1\frac{\partial V_{1n}}{\partial m} =\\ &V_{2n}(\frac{1}{RT_2}\frac{\partial p_2}{\partial m} + \frac{\rho_2(\gamma_2-1)}{T_2\gamma_2 R}V_{2m}\frac{\partial V_{2m}}{\partial m} + \frac{\rho_2(\gamma_2-1)}{T_2\gamma_2 R}V_{2n}\frac{\partial V_{2n}}{\partial m} + \frac{\rho(\gamma-1)}{T\gamma R}\frac{\partial Q_{c2}}{\partial m}) + \rho_2\frac{\partial V_{2n}}{\partial m}.\end{aligned} \tag{2.19}$$

Second, for the momentum conservation term,

$$\begin{aligned}&\frac{\partial p_1}{\partial l} + V_{1n}^2(\frac{1}{RT_1}\frac{\partial p_1}{\partial l} + \frac{\rho_1(\gamma_1-1)}{T_1\gamma_1 R}V_{1m}\frac{\partial V_{1m}}{\partial l} + \frac{\rho_1(\gamma_1-1)}{T_1\gamma_1 R}V_{1n}\frac{\partial V_{1n}}{\partial l} + \frac{\rho(\gamma-1)}{T\gamma R}\frac{\partial Q_{c1}}{\partial l}) + 2\rho_1 V_{1n}\frac{\partial V_{1n}}{\partial l} =\\ &\frac{\partial p_2}{\partial l} + V_{2n}^2(\frac{1}{RT_2}\frac{\partial p_2}{\partial l} + \frac{\rho_2(\gamma_2-1)}{T_2\gamma_2 R}V_{2m}\frac{\partial V_{2m}}{\partial l} + \frac{\rho_2(\gamma_2-1)}{T_2\gamma_2 R}V_{2n}\frac{\partial V_{2n}}{\partial l} + \frac{\rho(\gamma-1)}{T\gamma R}\frac{\partial Q_{c2}}{\partial l}) + 2\rho_2 V_{2n}\frac{\partial V_{2n}}{\partial l},\\ &\frac{\partial p_1}{\partial m} + V_{1n}^2(\frac{1}{RT_1}\frac{\partial p_1}{\partial m} + \frac{\rho_1(\gamma_1-1)}{T_1\gamma_1 R}V_{1m}\frac{\partial V_{1m}}{\partial m} + \frac{\rho_1(\gamma_1-1)}{T_1\gamma_1 R}V_{1n}\frac{\partial V_{1n}}{\partial m} + \frac{\rho(\gamma-1)}{T\gamma R}\frac{\partial Q_{c1}}{\partial m}) + 2\rho_1 V_{1n}\frac{\partial V_{1n}}{\partial m} =\\ &\frac{\partial p_2}{\partial m} + V_{2n}^2(\frac{1}{RT_2}\frac{\partial p_2}{\partial m} + \frac{\rho_2(\gamma_2-1)}{T_2\gamma_2 R}V_{2m}\frac{\partial V_{2m}}{\partial m} + \frac{\rho_2(\gamma_2-1)}{T_2\gamma_2 R}V_{2n}\frac{\partial V_{2n}}{\partial m} + \frac{\rho(\gamma-1)}{T\gamma R}\frac{\partial Q_{c2}}{\partial m}) + 2\rho_2 V_{2n}\frac{\partial V_{2n}}{\partial m}.\end{aligned} \tag{2.20}$$

Subsequently, equal tangential velocities are ensured:

$$\begin{aligned}\frac{\partial V_{1m}}{\partial l} &= \frac{\partial V_{2m}}{\partial l},\\ \frac{\partial V_{1m}}{\partial m} &= \frac{\partial V_{2m}}{\partial m}.\end{aligned} \tag{2.21}$$

Finally, we consider the chemical reaction term:

$$\begin{aligned}&\frac{\partial\rho_1}{\partial l}V_{1n}Z_1 + \frac{\partial V_{1n}}{\partial l}\rho_1 Z_1 + \frac{\partial Z_1}{\partial l}\rho_1 V_{1n} - \frac{\partial\rho_1}{\partial l}kZ_1\exp(-\frac{Ea}{R_1T_1}) - \frac{\partial Z_1}{\partial l}\rho_1 k\exp(-\frac{Ea}{R_1T_1}) + \frac{\partial T_1}{\partial l}\frac{Ea}{R_1T_1^2}\sigma_1 =\\ &\frac{\partial\rho_2}{\partial l}V_{2n}Z_2 + \frac{\partial V_{2n}}{\partial l}\rho_2 Z_2 + \frac{\partial Z_2}{\partial l}\rho_2 V_{2n} - \frac{\partial\rho_2}{\partial l}kZ_2\exp(-\frac{Ea}{R_2T_2}) - \frac{\partial Z_2}{\partial l}\rho_2 k\exp(-\frac{Ea}{R_2T_2}) + \frac{\partial T_2}{\partial l}\frac{Ea}{R_2T_2^2}\sigma_2,\\ &\frac{\partial\rho_1}{\partial m}V_{1n}Z_1 + \frac{\partial V_{1n}}{\partial m}\rho_1 Z_1 + \frac{\partial Z_1}{\partial m}\rho_1 V_{1n} - \frac{\partial\rho_1}{\partial m}kZ_1\exp(-\frac{Ea}{R_1T_1}) - \frac{\partial Z_1}{\partial m}\rho_1 k\exp(-\frac{Ea}{R_1T_1}) + \frac{\partial T_1}{\partial m}\frac{Ea}{R_1T_1^2}\sigma_1 =\\ &\frac{\partial\rho_2}{\partial m}V_{2n}Z_2 + \frac{\partial V_{2n}}{\partial m}\rho_2 Z_2 + \frac{\partial Z_2}{\partial m}\rho_2 V_{2n} - \frac{\partial\rho_2}{\partial m}kZ_2\exp(-\frac{Ea}{R_2T_2}) - \frac{\partial Z_2}{\partial m}\rho_2 k\exp(-\frac{Ea}{R_2T_2}) + \frac{\partial T_2}{\partial m}\frac{Ea}{R_2T_2^2}\sigma_2.\end{aligned} \tag{2.22}$$

2.4. *Three-dimensional curved detonation equations*

At this stage, the gradient relationships between the pre- and post-wave states of the 3D curved detonation wave have been derived (equations 2.19–2.22). However, the form is not concise enough. Let P denote the pressure gradient, U denote the velocity gradient in the l-direction, W denote the velocity gradient in the m-direction, and K denote the gradient of the chemical reaction process:

$$\begin{gathered}\frac{\partial p_1}{\partial l}=P_{1l},\frac{\partial p_1}{\partial m}=P_{1m},\frac{\partial V_{1m}}{\partial l}=U_{1m},\frac{\partial V_{1n}}{\partial l}=U_{1n},\frac{\partial V_{1n}}{\partial m}=W_{1n},\frac{\partial V_{1m}}{\partial m}=W_{1m},\frac{\partial Z_1}{\partial l}=K_{1l},\frac{\partial Z_1}{\partial m}=K_{1m}\\ \frac{\partial p_2}{\partial l}=P_{2l},\frac{\partial p_2}{\partial m}=P_{2m},\frac{\partial V_{2m}}{\partial l}=U_{2m},\frac{\partial V_{2n}}{\partial l}=U_{2n},\frac{\partial V_{2n}}{\partial m}=W_{2n},\frac{\partial V_{2m}}{\partial m}=W_{2m},\frac{\partial Z_2}{\partial l}=K_{2l},\frac{\partial Z_2}{\partial m}=K_{2m}\end{gathered} \tag{2.23}$$

Based on the above definition, the first term in equation (2.19) can be written as:

$$\begin{gathered}\frac{V_{1n}}{RT_1}P_{1l}+\frac{\rho_1(\gamma_1-1)}{T_1\gamma_1R}V_{1n}V_{1m}U_{1m}+(\frac{\rho_1(\gamma_1-1)}{T_1\gamma_1R}V_{1n}^2+\rho_1)U_{1n}+\frac{\rho_1(\gamma_1-1)}{T_1\gamma_1R}V_{1n}Q_0K_{1l}=\\ \frac{V_{2n}}{RT_2}P_{2l}+\frac{\rho_2(\gamma_2-1)}{T_2\gamma_2R}V_{2n}V_{2m}U_{2m}+(\frac{\rho_2(\gamma_2-1)}{T_2\gamma_2R}V_{2n}^2+\rho_2)U_{2n}+\frac{\rho_2(\gamma_2-1)}{T_2\gamma_2R}V_{2n}Q_0K_{2l}.\end{gathered} \tag{2.24}$$

We define the following symbols:

$$\begin{gathered}C_{11}=\frac{V_{1n}}{RT_1},C_{12}=\frac{\rho_1(\gamma_1-1)}{T_1\gamma_1R}V_{1n}V_{1m},C_{13}=(\frac{\rho_1(\gamma_1-1)}{T_1\gamma_1R}V_{1n}^2+\rho_1),C_{14}=\frac{\rho_1(\gamma_1-1)}{T_1\gamma_1R}V_{1n}Q_0,\\ C_{21}=\frac{V_{2n}}{RT_2},C_{22}=\frac{\rho_2(\gamma_2-1)}{T_2\gamma_2R}V_{2n}V_{2m},C_{23}=(\frac{\rho_2(\gamma_2-1)}{T_2\gamma_2R}V_{2n}^2+\rho_2),C_{24}=\frac{\rho_2(\gamma_2-1)}{T_2\gamma_2R}V_{2n}Q_0.\end{gathered} \tag{2.25}$$

Then, we can write:

$$C_{11}P_{1l}+C_{12}U_{1m}+C_{13}U_{1n}+C_{14}K_{1l}=C_{21}P_{2l}+C_{22}U_{2m}+C_{23}U_{2n}+C_{24}K_{2l}. \tag{2.26}$$

Similarly,

$$C_{11}P_{1m}+C_{12}W_{1m}+C_{13}W_{1n}+C_{14}K_{1m}=C_{21}P_{2m}+C_{22}W_{2m}+C_{23}W_{2n}+C_{24}K_{2m}. \tag{2.27}$$

Based on the above definitions, the first term in equation (2.20) can be stated as:

$$\begin{gathered}(1+\frac{V_{1n}^2}{RT_1})P_{1l}+\frac{\rho_1(\gamma_1-1)}{T_1\gamma_1R}V_{1n}^2V_{1m}U_{1m}+(\frac{\rho_1(\gamma_1-1)}{T_1\gamma_1R}V_{1n}^3+2\rho_1V_{1n})U_{1n}+\frac{\rho_1(\gamma_1-1)}{T_1\gamma_1R}V_{1n}^2Q_0K_{1l}=\\ (1+\frac{V_{2n}^2}{RT_2})P_{2l}+\frac{\rho_2(\gamma_2-1)}{T_2\gamma_2R}V_{2n}^2V_{2m}U_{2m}+(\frac{\rho_2(\gamma_2-1)}{T_2\gamma_2R}V_{2n}^3+2\rho_2V_{2n})U_{2n}+\frac{\rho_2(\gamma_2-1)}{T_2\gamma_2R}V_{2n}^2Q_0K_{2l}.\end{gathered} \tag{2.28}$$

Using the symbols:

$$\begin{gathered}C_{15}=1+\frac{V_{1n}^2}{RT_1},C_{16}=\frac{\rho_1(\gamma_1-1)}{T_1\gamma_1R}V_{1n}^2V_{1m},C_{17}=\frac{\rho_1(\gamma_1-1)}{T_1\gamma_1R}V_{1n}^3+2\rho_1V_{1n},C_{18}=\frac{\rho_1(\gamma_1-1)}{T_1\gamma_1R}V_{1n}^2Q_0,\\ C_{25}=1+\frac{V_{2n}^2}{RT_2},C_{26}=\frac{\rho_2(\gamma_2-1)}{T_2\gamma_2R}V_{2n}^2V_{2m},C_{27}=\frac{\rho_2(\gamma_2-1)}{T_2\gamma_2R}V_{2n}^3+2\rho_2V_{2n},C_{28}=\frac{\rho_2(\gamma_2-1)}{T_2\gamma_2R}V_{2n}^2Q_0,\end{gathered} \tag{2.29}$$

we obtain:

$$C_{15}P_{1l}+C_{16}U_{1m}+C_{17}U_{1n}+C_{18}K_{1l}=C_{25}P_{2l}+C_{26}U_{2m}+C_{27}U_{2n}+C_{28}K_{2l}. \tag{2.30}$$

Similarly,

$$C_{15}P_{1m} + C_{16}W_{1m} + C_{17}W_{1n} + C_{18}K_{1m} = C_{25}P_{2m} + C_{26}W_{2m} + C_{27}W_{2n} + C_{28}K_{2m}. \quad (2.31)$$

According to the above definitions, equation (2.21) can be written as:

$$\begin{gathered} U_{1m} = U_{2m}, \\ W_{1m} = W_{2m}. \end{gathered} \quad (2.32)$$

The first term in equation (2.22) can then be written as:

$$\begin{gathered} [V_{1n}Z_1 - kZ_1 \exp(-\frac{Ea}{R_1T_1})]\frac{1}{R_1T_1}\frac{\partial p_1}{\partial l} + ([V_{1n}Z_1 - kZ_1 \exp(-\frac{Ea}{R_1T_1})]\frac{\rho_1(\gamma_1 - 1)}{T_1\gamma_1R_1}V_{1m} - \\ \frac{\gamma_1 - 1}{\gamma_1R_1}\sigma_1\frac{Ea}{R_1T_1^2}V_{1m})\frac{\partial V_{1m}}{\partial l} + ([V_{1n}Z_1 - kZ_1 \exp(-\frac{Ea}{R_1T_1})]\frac{\rho_1(\gamma_1 - 1)}{T_1\gamma_1R_1}V_{1n} + \\ \rho_1Z_1 - \frac{\gamma_1 - 1}{\gamma_1R_1}\sigma_1\frac{Ea}{R_1T_1^2}V_{1n})\frac{\partial V_{1n}}{\partial l} \\ +([V_{1n}Z_1 - kZ_1 \exp(-\frac{Ea}{R_1T_1})]\frac{\rho_1(\gamma_1 - 1)}{T_1\gamma_1R_1}Q_0 + [\rho_1V_{1n} - \rho_1k \exp(-\frac{Ea}{R_1T_1})] - \frac{\gamma_1 - 1}{\gamma_1R_1}\sigma_1\frac{Ea}{R_1T_1^2}Q_0)\frac{\partial Z_1}{\partial l}. \end{gathered} \quad (2.33)$$

If we define:

$$\begin{gathered} C_{19} = [V_{1n}Z_1 - kZ_1 \exp(-\frac{Ea}{R_1T_1})]\frac{1}{R_1T_1}, \\ C_{110} = ([V_{1n}Z_1 - kZ_1 \exp(-\frac{Ea}{R_1T_1})]\frac{\rho_1(\gamma_1 - 1)}{T_1\gamma_1R_1}V_{1m} - \frac{\gamma_1 - 1}{\gamma_1R_1}\sigma_1\frac{Ea}{R_1T_1^2}V_{1m}), \\ C_{111} = [V_{1n}Z_1 - kZ_1 \exp(-\frac{Ea}{R_1T_1})]\frac{\rho_1(\gamma_1 - 1)}{T_1\gamma_1R_1}V_{1n} + \rho_1Z_1 - \frac{\gamma_1 - 1}{\gamma_1R_1}\sigma_1\frac{Ea}{R_1T_1^2}V_{1n}, \\ C_{112} = [V_{1n}Z_1 - kZ_1 \exp(-\frac{Ea}{R_1T_1})]\frac{\rho_1(\gamma_1 - 1)}{T_1\gamma_1R_1}Q_0 + [\rho_1V_{1n} - \rho_1k \exp(-\frac{Ea}{R_1T_1})] - \frac{\gamma_1 - 1}{\gamma_1R_1}\sigma_1\frac{Ea}{R_1T_1^2}Q_0 \\ C_{29} = [V_{2n}Z_2 - kZ_2 \exp(-\frac{Ea}{R_2T_2})]\frac{1}{R_2T_2}, \\ C_{210} = ([V_{2n}Z_2 - kZ_2 \exp(-\frac{Ea}{R_2T_2})]\frac{\rho_2(\gamma_2 - 1)}{T_2\gamma_2R_2}V_{2m} - \frac{\gamma_2 - 1}{\gamma_2R_2}\sigma_2\frac{Ea}{R_2T_2^2}V_{2m}), \\ C_{211} = [V_{2n}Z_2 - kZ_2 \exp(-\frac{Ea}{R_2T_2})]\frac{\rho_2(\gamma_2 - 1)}{T_2\gamma_2R_2}V_{2n} + \rho_2Z_2 - \frac{\gamma_2 - 1}{\gamma_2R_2}\sigma_2\frac{Ea}{R_2T_2^2}V_{2n}, \\ C_{212} = [V_{2n}Z_2 - kZ_2 \exp(-\frac{Ea}{R_2T_2})]\frac{\rho_2(\gamma_2 - 1)}{T_2\gamma_2R_2}Q_0 + [\rho_2V_{2n} - \rho_2k \exp(-\frac{Ea}{R_2T_2})] - \frac{\gamma_2 - 1}{\gamma_2R_2}\sigma_2\frac{Ea}{R_2T_2^2}Q_0, \end{gathered} \quad (2.34)$$

then:

$$C_{19}P_{1l} + C_{110}U_{1m} + C_{111}U_{1n} + C_{112}K_{1l} = C_{29}P_{2l} + C_{210}U_{2m} + C_{211}U_{2n} + C_{212}K_{2l}. \quad (2.35)$$

Similarly, in the m-direction,

$$C_{19}P_{1m} + C_{110}W_{1m} + C_{111}W_{1n} + C_{112}K_{1m} = C_{29}P_{2m} + C_{210}W_{2m} + C_{211}W_{2n} + C_{212}K_{2m}. \quad (2.36)$$

The complete 3D curved detonation equations can be described as:

$$\begin{gathered}
C_{11}P_{1l} + (C_{12} - C_{22})U_{1m} + C_{13}U_{1n} + C_{14}K_{1l} = C_{21}P_{2l} + C_{23}U_{2n} + C_{24}K_{2l},\\
C_{11}P_{1m} + (C_{12} - C_{22})W_{1m} + C_{13}W_{1n} + C_{14}K_{1m} = C_{21}P_{2m} + C_{23}W_{2n} + C_{24}K_{2m},\\
C_{15}P_{1l} + (C_{16} - C_{26})U_{1m} + C_{17}U_{1n} + C_{18}K_{1l} = C_{25}P_{2l} + C_{27}U_{2n} + C_{28}K_{2l},\\
C_{15}P_{1m} + (C_{16} - C_{26})W_{1m} + C_{17}W_{1n} + C_{18}K_{1m} = C_{25}P_{2m} + C_{27}W_{2n} + C_{28}K_{2m},\\
C_{19}P_{1l} + (C_{110} - C_{210})U_{1m} + C_{111}U_{1n} + C_{112}K_{1l} = C_{29}P_{2l} + C_{211}U_{2n} + C_{212}K_{2l},\\
C_{19}P_{1m} + (C_{110} - C_{210})W_{1m} + C_{111}W_{1n} + C_{112}K_{1m} = C_{29}P_{2m} + C_{211}W_{2n} + C_{212}K_{2m}.
\end{gathered} \tag{2.37}$$

In equation (2.37), there are six equations corresponding to six post-wave gradients, which means the equation is solvable. We believe that the advances offered by 3D curved detonation theory lie in two aspects: (i) previous theoretical studies on detonation have mostly focused on the zero-order parameters, and the solution was established through the Rankine–Hugoniot relations, whereas 3D curved detonation theory provides a higher-order research perspective by upgrading the research level from zero-order to first-order; (ii) 3D curved detonation theory expands the dimensions of the detonation research from the 2D planar/axisymmetric problem to the total 3D space.

3. Influence coefficient analysis of 3D curved detonation equations

3.1. *Derivation of influence coefficients*

Typically, the pre-wave gradient information is readily available. Thus, the post-wave gradient is the focal interest. We derive the influence coefficients of the post-wave gradient based on equation (2.37):

$$\begin{gathered}
C_{11}P_{1l} + (C_{12} - C_{22})U_{1m} + C_{13}U_{1n} + C_{14}K_{1l} = C_{21}P_{2l} + C_{23}U_{2n} + C_{24}K_{2l},\\
C_{15}P_{1l} + (C_{16} - C_{26})U_{1m} + C_{17}U_{1n} + C_{18}K_{1l} = C_{25}P_{2l} + C_{27}U_{2n} + C_{28}K_{2l},\\
C_{19}P_{1l} + (C_{110} - C_{210})U_{1m} + C_{111}U_{1n} + C_{112}K_{1l} = C_{29}P_{2l} + C_{211}U_{2n} + C_{212}K_{2l}.
\end{gathered} \tag{3.1}$$

For the first two terms of equation (3.1), after simplifying and eliminating terms, we have:

$$\begin{gathered}
(C_{11}C_{27} - C_{23}C_{15})P_{1l} + ((C_{12} - C_{22})C_{27} - (C_{16} - C_{26})C_{23})U_{1m} + (C_{13}C_{27} - C_{23}C_{17})U_{1n} +\\
(C_{14}C_{27} - C_{23}C_{18})K_{1l} = (C_{21}C_{27} - C_{23}C_{25})P_{2l} + (C_{24}C_{27} - C_{23}C_{28})K_{2l}.
\end{gathered} \tag{3.2}$$

Similarly, the last two terms of equation (3.1) can be written as:

$$\begin{gathered}
(C_{15}C_{211} - C_{27}C_{19})P_{1l} + ((C_{16} - C_{26})C_{211} - (C_{110} - C_{210})C_{27})U_{1m} + (C_{17}C_{211} - C_{27}C_{111})U_{1n} +\\
(C_{18}C_{211} - C_{27}C_{112})K_{1l} = (C_{25}C_{211} - C_{27}C_{29})P_{2l} + (C_{28}C_{211} - C_{27}C_{212})K_{2l}.
\end{gathered} \tag{3.3}$$

Continuing to eliminate unknowns yields:

$$(C_{24}C_{27} - C_{23}C_{28}) = C_{47}^{38}. \tag{3.4}$$

Then, equation (3.2) becomes:

$$\begin{gathered}
(C_{11}C_{27} - C_{23}C_{15})C_{811}^{712}P_{1l} + ((C_{12} - C_{22})C_{27} - (C_{16} - C_{26})C_{23})C_{811}^{712}U_{1m} + (C_{13}C_{27} -\\
C_{23}C_{17})C_{811}^{712}U_{1n} + (C_{14}C_{27} - C_{23}C_{18})C_{811}^{712}K_{1l} = (C_{21}C_{27} - C_{23}C_{25})C_{811}^{712}P_{2l} + C_{47}^{38}C_{811}^{712}K_{2l},
\end{gathered} \tag{3.5}$$

and equation (3.3) becomes:

$$\begin{gathered}(C_{15}C_{211}-C_{27}C_{19})C^{38}_{47}P_{1l}+((C_{16}-C_{26})C_{211}-(C_{110}-C_{210})C_{27})C^{38}_{47}U_{1m}+(C_{17}C_{211}-\\ C_{27}C_{111})C^{38}_{47}U_{1n}+(C_{18}C_{211}-C_{27}C_{112})C^{38}_{47}K_{1l}=(C_{25}C_{211}-C_{27}C_{29})C^{38}_{47}P_{2l}+C^{38}_{47}C^{712}_{811}K_{2l}.\end{gathered}\tag{3.6}$$

Subtracting one equation from the other and eliminating K_{2l} gives:

$$\begin{gathered}((C_{11}C_{27}-C_{23}C_{15})C^{712}_{811}-(C_{15}C_{211}-C_{27}C_{19})C^{38}_{47})P_{1l}\\ +(((C_{12}-C_{22})C_{27}-(C_{16}-C_{26})C_{23})C^{712}_{811}-((C_{16}-C_{26})C_{211}-(C_{110}-C_{210})C_{27})C^{38}_{47})U_{1m}\\ +((C_{13}C_{27}-C_{23}C_{17})C^{712}_{811}-(C_{17}C_{211}-C_{27}C_{111})C^{38}_{47})U_{1n}\\ +((C_{14}C_{27}-C_{23}C_{18})C^{712}_{811}-(C_{18}C_{211}-C_{27}C_{112})C^{38}_{47})K_{1l}\\ =((C_{21}C_{27}-C_{23}C_{25})C^{712}_{811}-(C_{25}C_{211}-C_{27}C_{29})C^{38}_{47})P_{2l}.\end{gathered}\tag{3.7}$$

Then, we obtain:

$$\begin{gathered}P_{2l}=((C_{11}C_{27}-C_{23}C_{15})C^{712}_{811}-(C_{15}C_{211}-C_{27}C_{19})C^{38}_{47})/((C_{21}C_{27}-C_{23}C_{25})C^{712}_{811}-(C_{25}C_{211}-\\ C_{27}C_{29})C^{38}_{47})P_{1l}+(((C_{12}-C_{22})C_{27}-(C_{16}-C_{26})C_{23})C^{712}_{811}-((C_{16}-C_{26})C_{211}-\\ (C_{110}-C_{210})C_{27})C^{38}_{47})/((C_{21}C_{27}-C_{23}C_{25})C^{712}_{811}-(C_{25}C_{211}-C_{27}C_{29})C^{38}_{47})U_{1m}\\ +((C_{13}C_{27}-C_{23}C_{17})C^{712}_{811}-(C_{17}C_{211}-C_{27}C_{111})C^{38}_{47})/((C_{21}C_{27}-C_{23}C_{25})C^{712}_{811}-\\ (C_{25}C_{211}-C_{27}C_{29})C^{38}_{47})U_{1n}+((C_{14}C_{27}-C_{23}C_{18})C^{712}_{811}-(C_{18}C_{211}-C_{27}C_{112})C^{38}_{47})/\\ ((C_{21}C_{27}-C_{23}C_{25})C^{712}_{811}-(C_{25}C_{211}-C_{27}C_{29})C^{38}_{47})K_{1l}.\end{gathered}\tag{3.8}$$

Using the definitions:

$$\begin{aligned}J_p&=((C_{11}C_{27}-C_{23}C_{15})C^{712}_{811}-(C_{15}C_{211}-C_{27}C_{19})C^{38}_{47})/((C_{21}C_{27}-C_{23}C_{25})C^{712}_{811}-\\ &\qquad(C_{25}C_{211}-C_{27}C_{29})C^{38}_{47}),\\ L_p&=(((C_{12}-C_{22})C_{27}-(C_{16}-C_{26})C_{23})C^{712}_{811}-((C_{16}-C_{26})C_{211}-(C_{110}-C_{210})C_{27})C^{38}_{47})\\ &\qquad/((C_{21}C_{27}-C_{23}C_{25})C^{712}_{811}-(C_{25}C_{211}-C_{27}C_{29})C^{38}_{47}),\\ I_p&=((C_{13}C_{27}-C_{23}C_{17})C^{712}_{811}-(C_{17}C_{211}-C_{27}C_{111})C^{38}_{47})/((C_{21}C_{27}-C_{23}C_{25})C^{712}_{811}-\\ &\qquad(C_{25}C_{211}-C_{27}C_{29})C^{38}_{47}),\\ N_p&=((C_{14}C_{27}-C_{23}C_{18})C^{712}_{811}-(C_{18}C_{211}-C_{27}C_{112})C^{38}_{47})/((C_{21}C_{27}-C_{23}C_{25})C^{712}_{811}-\\ &\qquad(C_{25}C_{211}-C_{27}C_{29})C^{38}_{47}),\end{aligned}\tag{3.9}$$

the following can be derived:

$$P_{2l}=J_pP_{1l}+L_pU_{1m}+I_pU_{1n}+N_pK_{1l}.\tag{3.10}$$

The other expression can be obtained by applying a similar approach (the detailed derivation can be found in Appendix C). The final results are:

$$K_{2l}=J_kP_{1l}+L_kU_{1m}+I_kU_{1n}+N_kK_{1l},\tag{3.11}$$

$$U_{2l}=J_uP_{1l}+L_uU_{1m}+I_uU_{1n}+N_uK_{1l}.\tag{3.12}$$

In this way, the 3D curved detonation equations are given in the form of influence coefficients as:

$$\begin{aligned} P_{2l} &= J_p P_{1l} + L_p U_{1m} + I_p U_{1n} + N_p K_{1l}, \\ K_{2l} &= J_k P_{1l} + L_k U_{1m} + I_k U_{1n} + N_k K_{1l}, \\ U_{2l} &= J_u P_{1l} + L_u U_{1m} + I_u U_{1n} + N_u K_{1l}. \end{aligned} \tag{3.13}$$

Considering that the partial derivates in the m-direction have the same form as those in the l-direction, we obtain:

$$\begin{aligned} P_{2m} &= J_p P_{1m} + L_p W_{1m} + I_p W_{1n} + N_p K_{1m}, \\ K_{2m} &= J_k P_{1m} + L_k W_{1m} + I_k W_{1n} + N_k K_{1m}, \\ U_{2m} &= J_u P_{1m} + L_u W_{1m} + I_u W_{1n} + N_u K_{1m}. \end{aligned} \tag{3.14}$$

The physical significance of the influence coefficients is illustrated below using P_{2l} as an example. J_p reflects the gradient of the incoming pressure in the l-direction with respect to the gradient of the post-wave pressure in the l-direction (P_{2l}); L_p indicates the gradient of the incoming tangential velocity in the m-direction with respect to P_{2l}; I_p is the gradient of the incoming tangential velocity in the n-direction with respect to P_{2l}; and N_p reveals the gradient of the incoming chemical reaction process in the l-direction with respect to P_{2l}.

3.2. *Influence coefficient analysis*

Once the influence coefficients outlined in equations (3.13) and (3.14) have been obtained, the specific values of each coefficient can be determined. The magnitude of these coefficients signifies the relationship between the gradients and holds significant value when analysing the aerodynamic principles underlying the detonation process. Consequently, thorough analysis and investigation are imperative. Through the theoretical derivation presented in this article, which employs a single-step chemical reaction model, the parameters of the incoming flow are determined based on dimensionless parameters as follows:

$$p_1 = 1, T_1 = 1, M_1 = 10, \gamma_1 = 1.3, R_1 = 0.99, Ea = 20, Q_0 = 40, Z_1 = 1, k = 2 \times 10^3. \tag{3.15}$$

Three different 3D curved wave geometries are considered in this paper. The first type is a curved wave with curvature in the plane, the second type is a curved wave with axisymmetric curvature in the axial direction, and the third type is a bi-directional curved wave with curvature in both the planar and axisymmetric directions. Thus, the function with planar curvature is given as

$$F = 0.5z^2 - x, z\&y \in [0.8\ 1], \tag{3.16}$$

where F is the wave function and x, y, z denote the three Cartesian coordinates. With such a 3D wave function, the influence coefficients of the post-wave pressure and velocity gradients are as shown in figures 2 and 3, respectively. In figure 2, J_p and N_p are positive within the entire x-coordinate range, which means that the pre-wave pressure gradient and the process gradient enhance the post-wave pressure gradient. L_p and I_p change from positive to negative, which indicates that the velocity gradient changes from a positive to a negative gain on the pressure gradient as the x-coordinate decreases. In terms of the magnitude of the influence coefficient, the process gradient is the largest, which means that the change in the process gradient has the most dramatic impact on the post-wave pressure gradient. Observing the changing patterns of the four curves shows that as the coordinates decrease, all influence coefficients exhibit a downward trend. This means that a larger detonation wave is less susceptible to the various pre-wave gradients. This is consistent with the conclusion of the 2D curved shock theory (Mölder 2016). In figure 3, J_u, L_u, I_u, N_u are all positive,

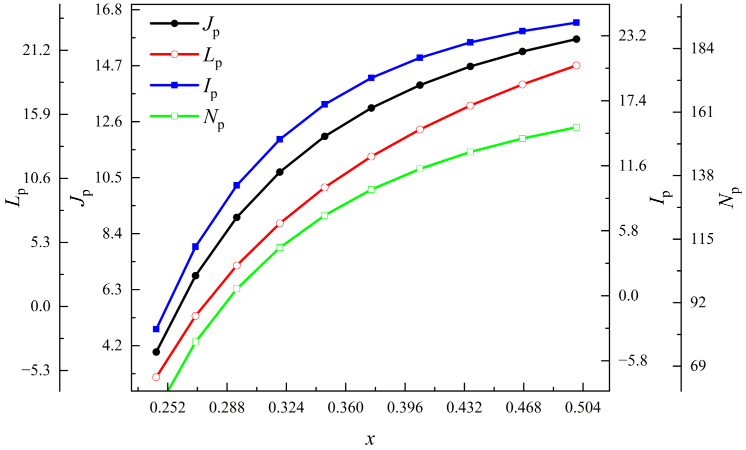

Figure 2: Influence coefficient of pressure gradient in the curved detonation wave with planar curvature.

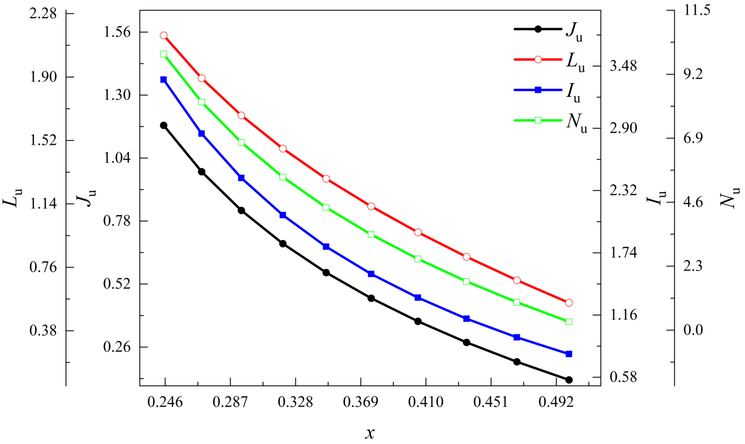

Figure 3: Influence coefficient of velocity gradient in the curved detonation wave with planar curvature.

which means that the pre-wave pressure gradient, velocity gradient, and process gradient all increase the post-wave velocity gradient in this coordinate range. Similarly, the process gradient change has the most significant effect on the post-wave velocity gradient. All four curves show an increasing trend as the coordinates decrease, which means that the velocity gradient is more likely to be affected by the pre-wave gradient in a more angular detonation wave. The above pattern of change provokes two questions: (i) why does the process gradient have the most significant influence? and (ii) why do the coefficients of influence of the pressure and velocity gradients exhibit different patterns of change? Correspondingly, the following conjectures are stated. (1) For a unit change in the process gradient, the resulting zero-order parameter change is greater than a unit change in the zero-order parameter. For example, under the above conditions, if Z_2=0, i.e. in the case of shock waves, the corresponding post-wave pressure can be calculated as p_2=56.39 using the Rankine–Hugoniot relation; when Z_2=1, i.e. in the case of detonation, the post-wave pressure p_2= 50.17. In other words,

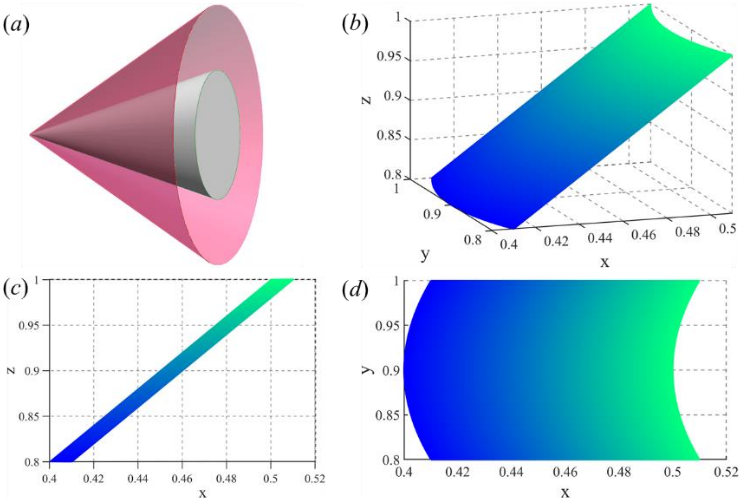

Figure 4: Three-dimensional curved detonation waves with only transversal curvature: (*a*) geometric structure with induced mechanism, (*b*) wave surface function, (*c*) projection of the wave surface in the xz-direction, and (*d*) projection of the wave surface in the xy-direction.

$dZ = 1$, the corresponding $dp > 1$. (2) Because the individual coefficients are obtained by very complex calculations, it is difficult to intuitively obtain a linear relationship between the influence coefficients and a specific physical quantity. However, some insight may be gained from the variation of the zero-order parameters. When the wave angle increases, the pressure after the detonation wave is followed by an increase, while the velocity is followed by a decrease. The zero-order parameters between the opposite pattern of change may lead to the first-order gradient influence coefficients between the reverse change.

As shown in figure 4(a), axisymmetric detonation exhibits transversal curvature in the l-direction and an absence of curvature in the m, n-directions. If the function of the 3D wave surface is given as:

$$F(x) = 0.5z - x + (y - 0.9)^2, z\&y \in [0.8\ 1], \tag{3.17}$$

the rest of the incoming flow parameters are consistent with the previous section, and the influence coefficients can be obtained as shown in figures 5 and 6. In figure 5, all the influence coefficients of the post-wave pressure gradient are positive, which indicates that, at this point, the pre-wave pressure, velocity, and process gradients increase the post-wave pressure gradient. Through observation, it can be inferred that these influence coefficients are symmetric and reach the minimum value at the symmetric point. This law implies that, for an axisymmetric detonation wave surface at the symmetry point, the post-wave pressure gradient is minimally affected by each of the pre-wave gradients. In figure 6, the individual influence coefficients of the velocity gradient are also positive and symmetric. In contrast to the pressure gradient, the individual influence coefficients are maximized at the point of symmetry. This pattern implies that, for an axisymmetric detonation wave, the post-wave velocity gradient at the point of symmetry is maximized by the pre-wave gradients. To explore the reasons for this, we plot the wave angle and curvature in figure 7.

In figure 7, the horizontal coordinate is y, the black curve is the x-coordinate, the red curve is the wave angle θ, and the blue curve is the curvature S_b. According to figure 7, the wave angle and curvature attain their maximum values at the symmetry point. The wave angle reaching its extreme value means that a larger zero-order parameter can be obtained here,

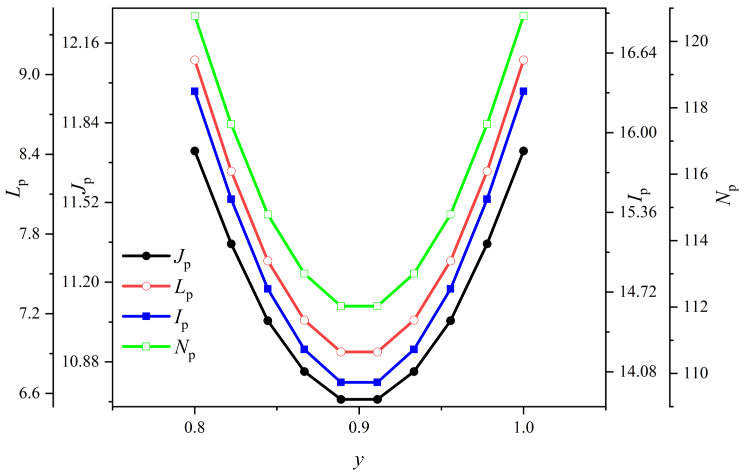

Figure 5: Influence coefficients of post-wave pressure gradients for axisymmetric curved detonation waves.

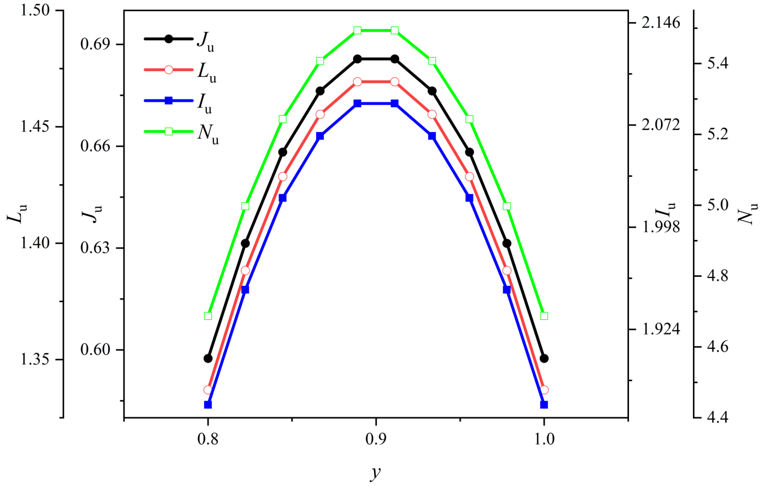

Figure 6: Influence coefficients of post-wave velocity gradients for axisymmetric curved detonation waves.

and the curvature also taking its extreme value indicates the maximum rate of change of the wave angle, and thus the largest rate of change of the zero-order parameter.

Next, a wave function with bi-directional curvature is given as:

$$F(x) = 0.5z^2 - x + (y - 0.9)^2, z\&y \in [0.81]. \tag{3.18}$$

In the previous examples, the distribution law of the influence coefficients in the x, y-directions was discussed. In this case, the distribution law of the influence coefficients in the z-direction is analysed. First, the pressure gradient distribution law in the z-direction is plotted in figure 8. The individual influence coefficients increase gradually along the z-direction and each influence coefficient is positive, indicating that the pre-wave pressure, velocity, and process gradients all increase the post-wave pressure gradient in this range of z. Again, the process gradient is the largest and the pressure gradient is the smallest among the influence

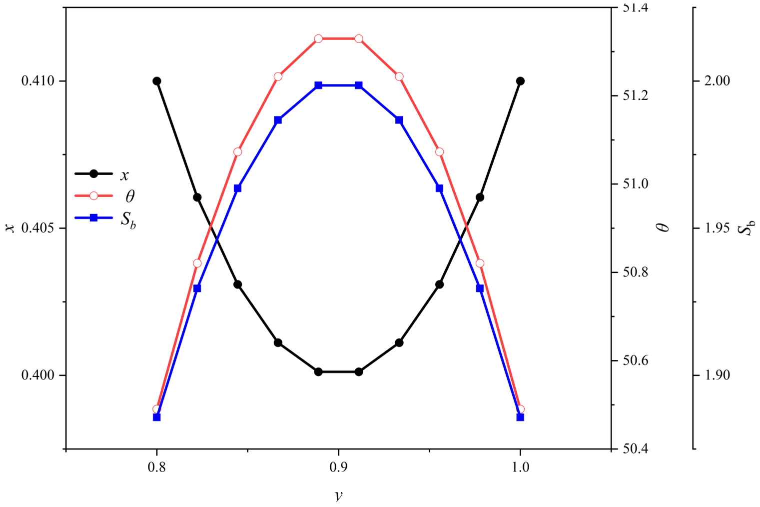

Figure 7: Wave angle and curvature distributions for axisymmetric curved detonation waves.

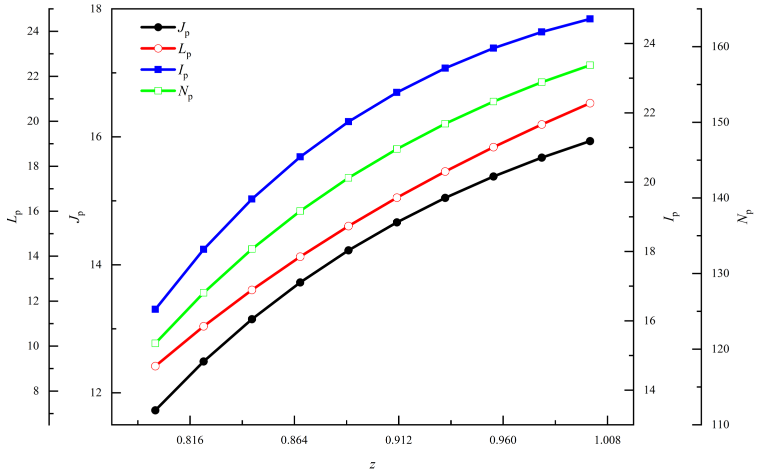

Figure 8: Influence coefficients of post-wave pressure gradients along the z-direction for a 3D curved detonation wave.

coefficients. This means that the chemical reaction process in the pre-wave remains the most significant influence on the post-wave pressure gradient. Next, the distribution pattern of the influence coefficients of the velocity gradient in the z-direction is analysed. In figure 9, the individual influence coefficients of the velocity gradient decrease as z increases. This indicates that the velocity gradient is more likely to be affected at lower locations and less affected at higher locations. Among the many influencing coefficients, the process gradient is still dominant, except for the normal and tangential velocities, and the pressure gradient has the least impact. The distribution of the influence coefficients in the z-direction is similar to that in the x-direction when the plane is curved. This is because the wave function is the same in the xz-plane, as shown in figure 10. The resulting changes in wave angle and curvature in the z-direction are also similar, thus leading to similar influence coefficients.

These trends are mainly caused by the geometrical features of the wave. To eliminate

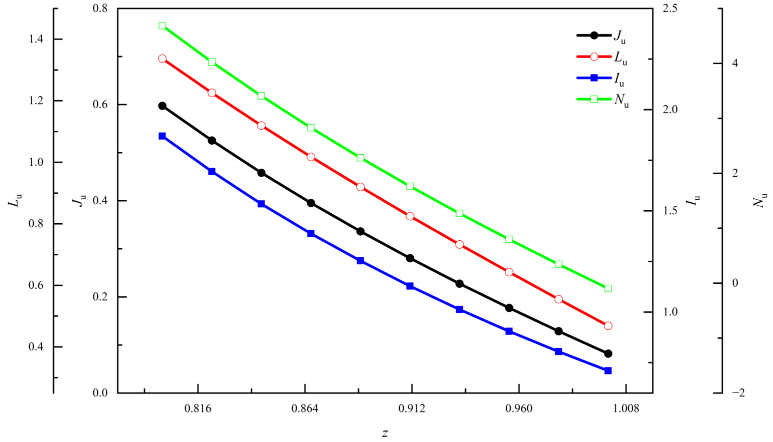

Figure 9: Influence coefficients of post-wave velocity gradients along the z-direction for a 3D curved detonation wave.

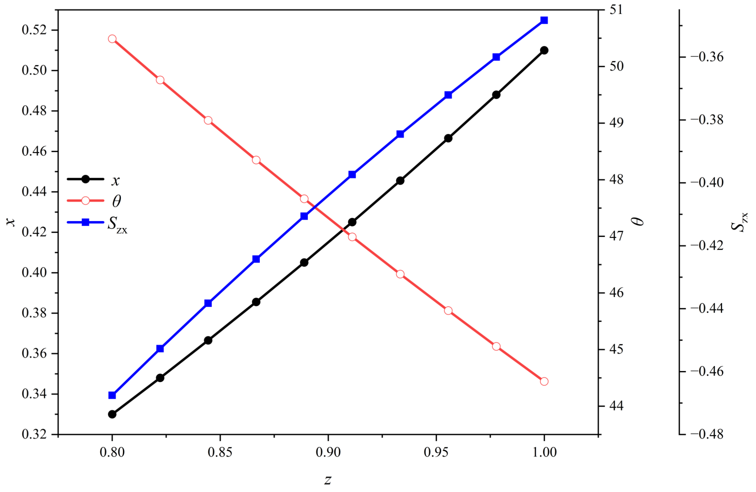

Figure 10: Distribution pattern of wave angle and curvature along the z-direction for a 3D curved detonation wave.

the influence of the geometrical features, the wave angles are plotted separately from the influence coefficients in figure 11. The influence coefficient is positive and decreases gradually with increasing wave angle in the xz-plane, while the curvature is negative and increases gradually in absolute value. In the xy-plane, an increase in the wave angle causes the influence coefficient to gradually decrease and the curvature to increase. There is a negative correlation between the wave angle and the influence coefficient, which means that the pre-wave pressure gradient has less influence on the post-wave pressure gradient at larger wave angles. The reason why the influence coefficient exhibits a different change in each direction may be related to the different curvature (blue line) in the two directions. The next example analyses J_u using a similar analytical method. In figure 12, the influence coefficient is positive and gradually increases with increasing wave angle in the xz-plane; similarly, the influence coefficient gradually increases with increasing wave angle in the xy plane. These

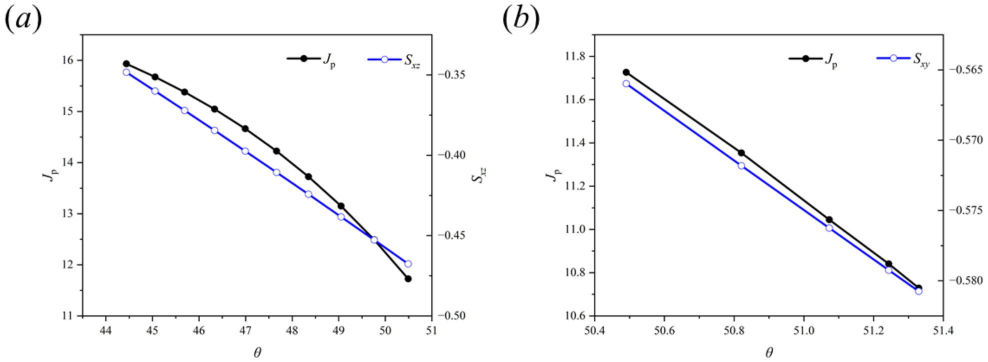

Figure 11: Pattern of variation between post-wave gradient and the influence coefficient J_p of curvature and wave angle in a 3D curved detonation wave.

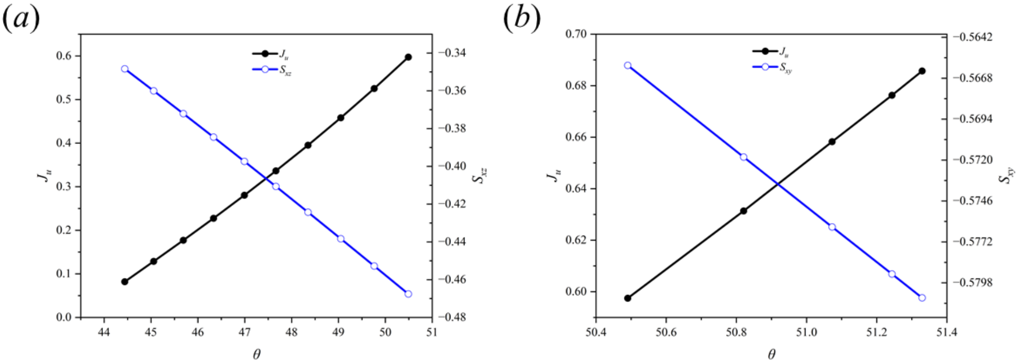

Figure 12: Pattern of variation between post-wave gradient and influence coefficient J_u of curvature and wave angle in a 3D curved detonation wave.

changes imply that the pre-wave pressure gradient has a greater effect on the post-wave velocity gradient at larger wave angles.

4. Post-wave gradient analysis of 3D curved detonation equations

Following the detailed analysis of the influence coefficients in the previous section, the post-wave pressure and velocity gradient parameters are now discussed. Combined with the zero-order parameters, the post-wave aerodynamic parameters are quantitatively analysed.

4.1. *Post-wave temperature and density gradients*

Among the basic aerodynamic parameters, the pressure and velocity have already been discussed, leaving the density and the temperature. The partial derivatives of the density can be obtained from equation (2.18). According to equations (2.16) and (2.17), the temperature gradients can be derived as follows:

$$\begin{aligned} \frac{\partial T}{\partial l} &= -(V_m\frac{\partial V_m}{\partial l}+V_n\frac{\partial V_n}{\partial l}+\frac{\partial Q_c}{\partial l})\frac{\gamma-1}{\gamma R}, \\ \frac{\partial T}{\partial m} &= (V_m\frac{\partial V_m}{\partial m}+V_n\frac{\partial V_n}{\partial m}+\frac{\partial Q_c}{\partial m})\frac{\gamma-1}{\gamma R}. \end{aligned} \tag{4.1}$$

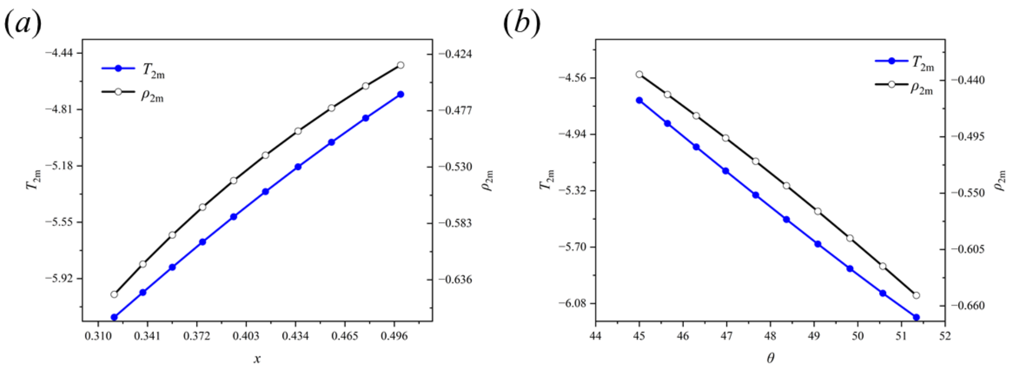

Figure 13: Gradients of temperature and density along the m-direction: (a) x-coordinate; (b) wave angle.

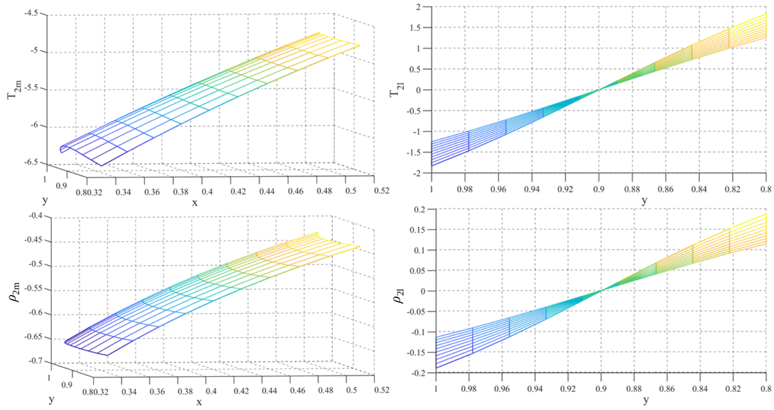

Figure 14: Gradient distributions of temperature and density in the m- and l-directions.

To explore the variation of the temperature gradients, the distribution of the temperature gradients is calculated in the 2D and 3D curved cases. For a 2D curved wave, the gradients of temperature and density along the m-direction are plotted in figure 13. In figure 13, the gradients of density and temperature along the m-direction are both negative, which indicates that there is a tendency for both temperature and density to decrease. The gradient change is positively correlated with the x-coordinate and negatively correlated with the wave angle. The magnitudes require careful attention because these values are negative. Both reach their absolute maximum at the maximum angle, which implies that the changes in temperature and density are more drastic in stronger detonation waves. The second case is the more complex 3D curved wave, for which the temperature and density gradients in the m- and l-directions are shown in figure 14. The temperature and density are negative in the m-direction, and the gradient changes in the l-direction are similarly characterized by reverse symmetry, which again implies that the temperature and density peak at the stationary point.

4.2. *Post-wave gradient analysis in curved detonation waves*

The first-order gradient variation after the detonation wave is now analysed for planar, axisymmetric, and 3D cases. Before calculating the first-order gradients, the zero-order parameters are presented in figure 15. The calculation conditions remain the same as for the

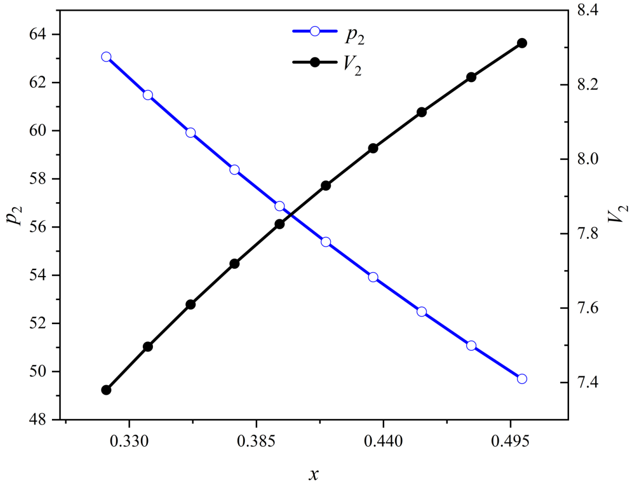

Figure 15: Post-wave pressure and velocity distributions along the x-direction for a curved wave with planar curvature.

previous influence coefficient analysis. In figure 15, the pressure gradually decreases with increasing x-coordinate and the velocity gradually increases with increasing x-coordinate. This is because the wave angle decreases gradually as the x-coordinate increases.

The post-wave gradients are shown in figure 16. The green curve shows the post-wave pressure gradient along the m-direction, with negative values indicating that the pressure is decreasing. This curve also shows that the amplitude of the gradient gradually increases as the wave angle increases. This implies that the pressure change along the m-direction is increasing, i.e. the pressure exhibits a greater decrease after a stronger detonation wave. This is consistent with the influence coefficient change. The red curve is the gradient of the n-direction velocity component in the m-direction, and the negative value again indicates that this velocity component is decreasing in the m-direction. The absolute value increases with the wave angle, similar to the pressure component. In contrast, the blue curve, representing the velocity component in the m-direction, exhibits positive values, indicating that the post-wave velocity component increases at that point.

The post-wave zero-order parameters and first-order gradients of an axisymmetric curved wave are shown in figure 17. The pressure first rises and then falls, attaining its peak value at the symmetry point. In contrast, the pressure gradient (black curve in figure 17) is positive to the left of the symmetry point, indicating that the pressure increases in the y-direction, and negative to the right of the symmetry point, indicating that the pressure decreases in the y-direction. Therefore, the peak is reached at the symmetry point. That is, the trend of the first-order gradient is consistent with the change in the zero-order parameter, indicating that the gradient calculated in this paper is reasonable.

For a 3D curved wave, the post-wave zero-order parameters are shown in figure 18. Using the same computational conditions as for the influence coefficient analysis, the post-wave gradients are shown in figure 19. The gradients have m- and l-directions, and the x- and y-coordinates have two directions. In figure 19, the gradients of pressure and normal velocity along the m-direction follow a similar pattern in the x-direction, both increasing gradually. The opposite is true for the tangential velocity, as analysed in the previous section. In the y-direction, all three gradients are symmetric. In figure 20, the gradient of pressure along the l-direction exhibits directional symmetry in the y-direction. The gradient of tangential

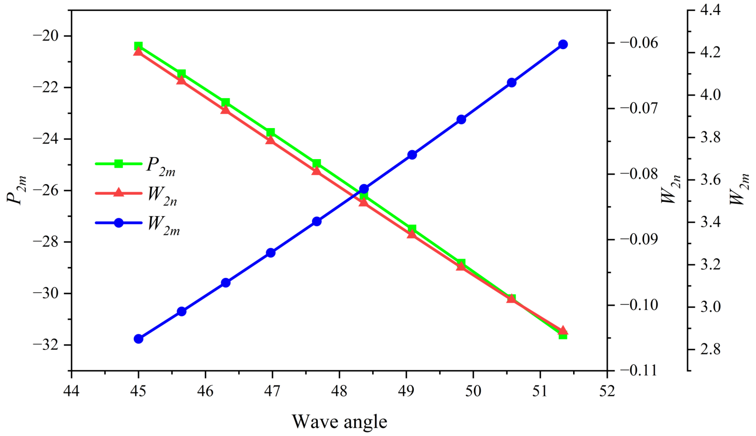

Figure 16: Post-wave aerodynamic parameter gradients with wave angle for a curved detonation wave with planar curvature.

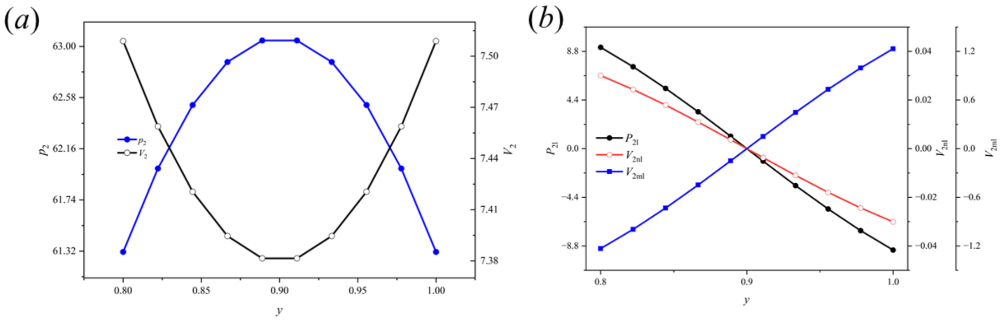

Figure 17: Post-wave pressure and velocity gradients along the y-direction for an axisymmetric curved wave.

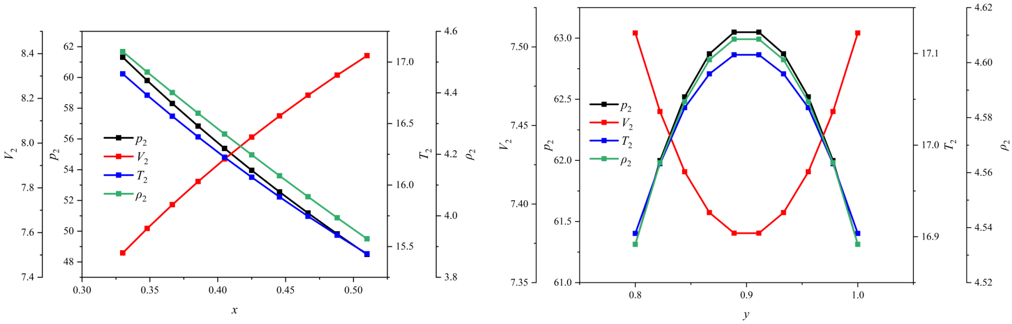

Figure 18: Distribution of post-wave zero-order parameters along x- and y-directions for a 3D curved wave.

velocity in the y-direction varies in the opposite direction to the pressure. For a clearer view, the gradient is now expanded in each of the two directions along xy, yielding figures 21 and 22.

In figure 21, the absolute values of the gradients of pressure and normal velocity in the m-direction decrease as x increases, which is similar to the pattern observed in the previous

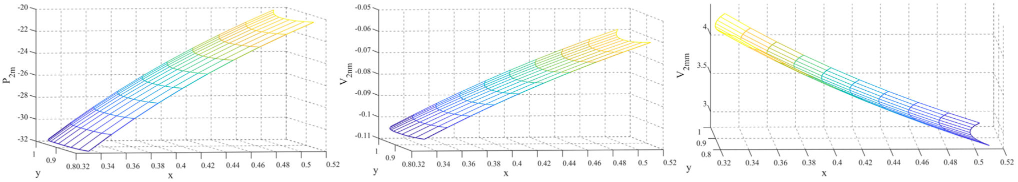

Figure 19: Post-wave gradient distributions on a 3D surface: (*a*) pressure gradient along m-direction, (*b*) normal velocity gradient along m-direction, (*c*) tangential velocity gradient along m-direction.

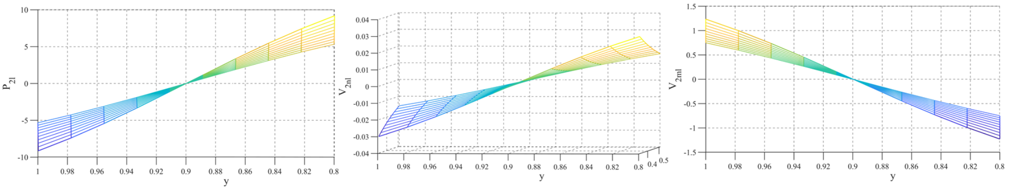

Figure 20: Post-wave gradient distributions on a 3D surface: (*a*) pressure gradient along l-direction, (*b*) normal velocity gradient along l-direction, (*c*) tangential velocity gradient along l-direction.

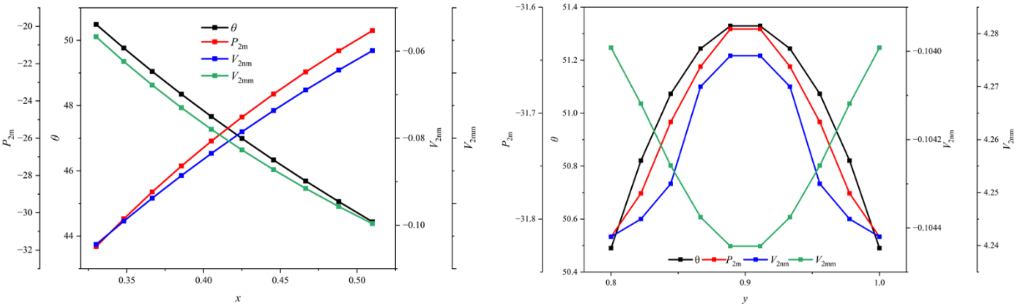

Figure 21: Individual gradients in the m-direction expanded along the xy-plane.

section. In particular, the gradients are symmetric in the y-direction, and this symmetry arises from the symmetry of the wave angle. The wave angle reaches a maximum at the centre of symmetry, $y = 0.9$, and decreases on either side. At that point, the absolute values of the pressure and normal velocity (tangential velocity) gradients are minimized, implying that the rate of decrease (increase) of the pressure and normal velocity (tangential velocity) along the m-direction is minimal. In figure 22, the pressure and normal velocity gradients are positive and the tangential velocity gradient is negative. This means that the pressure and normal velocity at these points tend to increase along the l-direction while the tangential velocity tends to decrease. The absolute values of the pressure and normal velocity gradients in the l-direction decrease as x increases, indicating that the rate of increase is slowing down. In the y-direction, although the wave angle is symmetric, the individual gradients exhibit reverse symmetry at this point. The change from positive to negative pressure and normal velocity indicates that, in the interval 0.8–0.9, there is a tendency for these quantities to increase along the l-direction, while in the interval 0.9–1.0, there is a tendency for them to decrease along the l-direction. The change in tangential velocity has the opposite trend.

Combined with figures 21 and 22, at the starting point of x and the midpoint of y (stationary point) (i.e. $x = 0.33$, $y = 0.9$), the gradient of pressure along the m-direction is negative and

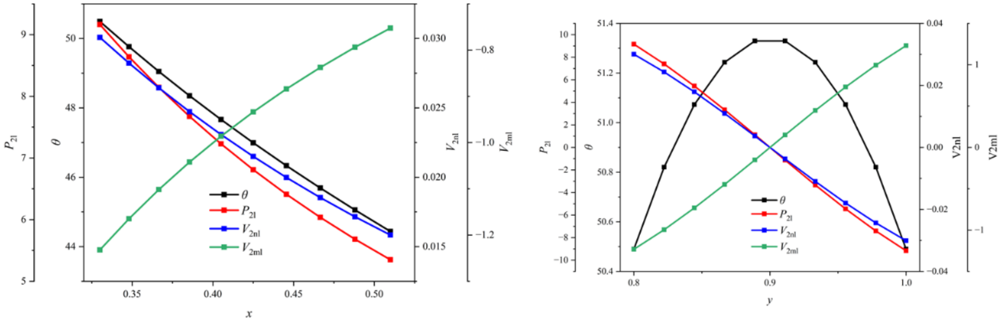

Figure 22: Individual gradients in the l-direction expanded along the xy-plane.

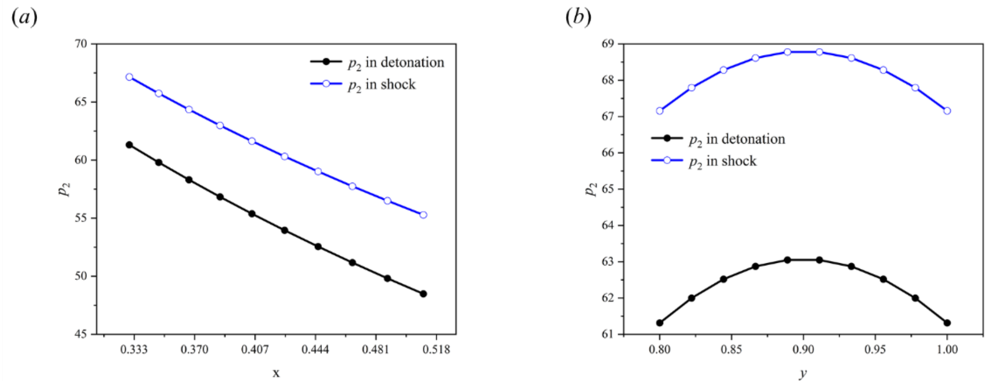

Figure 23: Post-wave pressure of the shock/detonation wave: (a) x-direction, (b) y-direction.

the absolute value decreases with increasing x. This indicates that the pressure gradually decreases from this point onwards. The gradient of pressure along the l-direction in the range of 0.8–0.9 is positive and the absolute value decreases, indicating that the pressure gradually increases from this point onwards. By 0.8–1.0, the pressure decreases from this point onwards. The pressure gradient along the l-direction in the range of 0.8–0.9 is positive and the absolute value decreases gradually, indicating that the pressure gradually increases from this point onwards; in the interval 0.9–1.0, the pressure gradient becomes negative, indicating that the pressure gradually decreases from this point onwards. Combining these three stages of the changes in gradient, we can deduce that the pressure reaches a peak at the stationary point.

4.3. *Post-wave gradients compared with shock waves*

The similarity between shock and detonation waves has led to many comparisons. As the zero-order parameters have been the subject of previous research, this paper describes a comparison of the first-order gradients. To facilitate the comparison, both the shock and detonation have the same wave function (equation 3.16) and the same incoming flow conditions (equation 3.15). The post-wave zero-order pressures of shock and detonation are shown in figure 23, where the black and blue lines denote the detonation and shock pressures, respectively. In both directions, the pressure of the detonation is significantly smaller than that of the shock because the combustion process causes the pressure to drop.

The post-wave pressure gradients of shock/detonation can be solved using the 3D curved

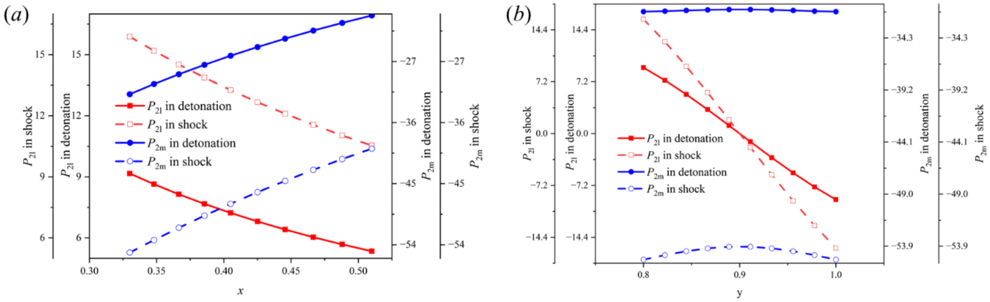

Figure 24: Post-wave pressure gradient of the shock/detonation wave: (*a*) x-direction, (*b*) y-direction.

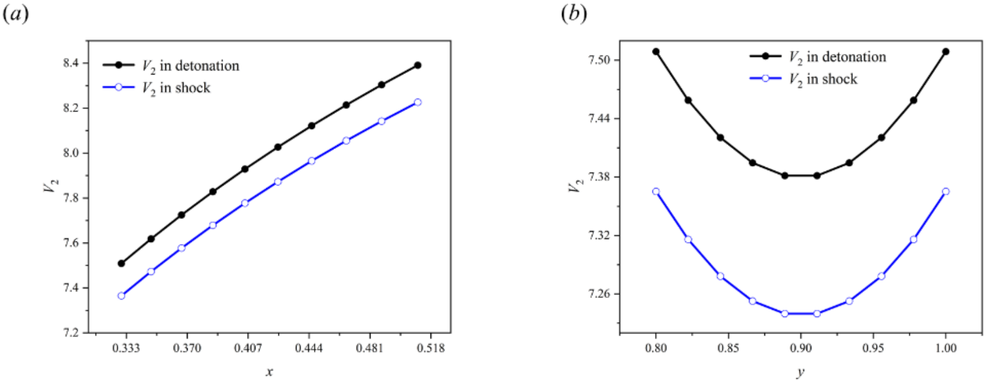

Figure 25: Post-wave velocity of the shock/detonation wave: (*a*) x-direction, (*b*) y-direction.

detonation theory proposed in this paper, as shown in figure 24, where the solid lines indicate the detonation and the dashed lines represent the shock. The red curves are the pressure gradients in the l-direction. The pressure gradient of the shock in the l-direction is significantly larger than that of the detonation wave. The blue curves denote the pressure gradient in the m-direction, which is again larger for the shock than for the detonation. Considering that the wave surface function is the same, i.e. the wave angle is the same, and the incoming flow parameters are also the same, the post-wave zero-order parameters lead to the differences in the first-order gradients. From a different perspective, the shock can be viewed as a detonation wave with a larger wave angle, which is consistent with the conclusions of figure 21.

The difference in velocity gradients between the shock and detonation is also worth investigating. As shown in figure 25, the velocity of the detonation is greater than that of the shock. The tangential velocity gradients of the shock and detonation are the same because the wave curvature and the incoming flow parameters are the same. Thus, the post-wave tangential velocity gradient is consistent with the pre-wave tangential velocity gradient (equation 2.32). Therefore, only the normal velocity gradient is studied, as shown in figure 26. The gradient of the normal velocity in the l-direction of the detonation (shock) wave is always positive (negative), whereas the normal velocity gradient of the detonation (shock) in the m-direction is always negative (positive). As for the y-direction, the normal velocity gradients in the l-direction for both the detonation and shock are symmetric about $y = 0.9$, as expected. However, the normal velocity gradient in the l-direction shows a completely different pattern

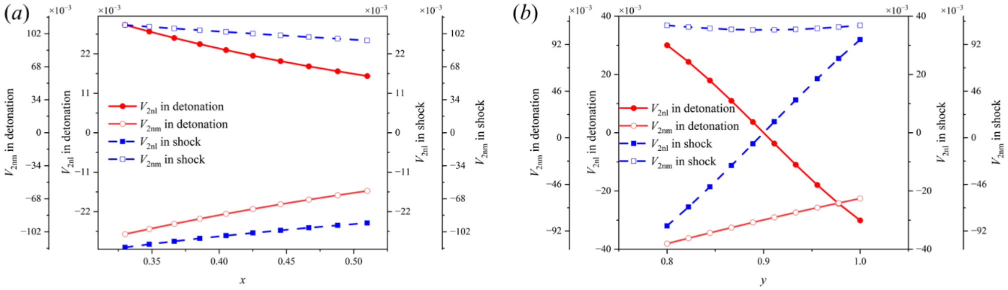

Figure 26: Post-wave normal velocity gradient of the shock/detonation wave: (*a*) x-direction, (*b*) y-direction.

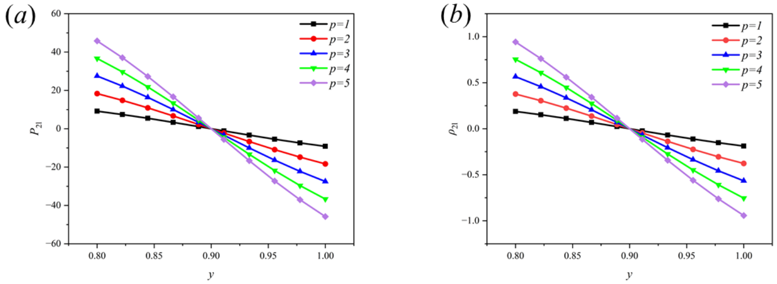

Figure 27: Post-wave gradients for different incoming pressures: (*a*) pressure gradient, (*b*) density gradient.

of variation in the y-direction, with the gradient decreasing in the negative range for the detonation and remaining symmetric about $y = 0.9$ in the positive range for the shock. Some of the gradient variations are comprehensible, but others remain unclear and require further study.

5. Applications of 3D curved detonation equations

The 3D curved detonation equations systematically solve the post-wave gradient parameters of the detonation, which provides a new perspective and a favourable method for detonation. In addition to the above analysis of influence coefficients and post-wave gradients, the equations can be used for the following applications.

5.1. *Influence of incoming parameters and energy release on post-wave gradients*

Considering the importance of the incoming parameters on detonation, we now explore the effect on the post-wave gradients. First, the post-wave gradient parameters under different incoming pressures are shown in figure 27. We found that the gradients of velocity and temperature are not affected by pressure changes, and only the pressure and density gradients change. In figure 27, the pressure and density post-wave gradients increase monotonically with increasing pressure. To clarify the reason for this, we present the equation governing the detonation wave relationship for variable specific heat ratios:

$$\frac{\rho_2}{\rho_1}{=}X, \frac{p_2}{p_1} = 1 + \gamma_1 {M_1}^2 sin^2\theta(1 - X), \frac{V_{2n}}{V_{1n}} = \frac{1}{X}, \tag{5.1}$$

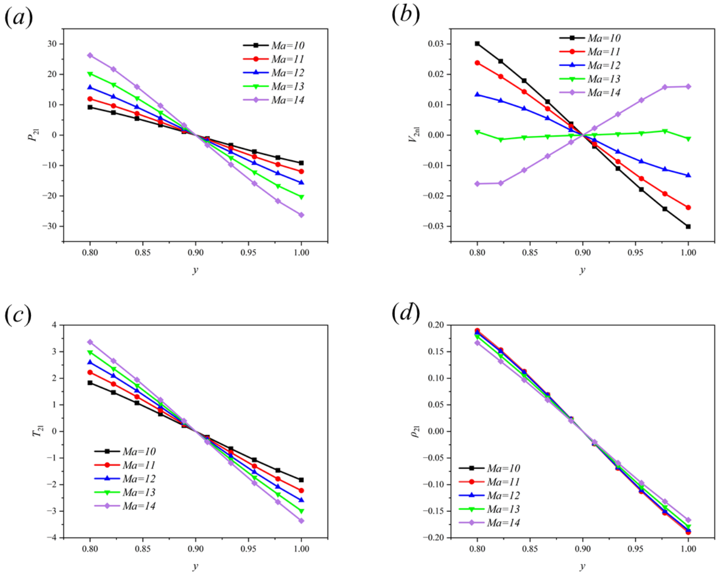

Figure 28: Post-wave gradients for different incoming Mach numbers: (*a*) pressure, (*b*) velocity, (*c*) temperature, and (*d*) density.

where

$$X = \frac{(1+\gamma_1 M_{1n}^2)\frac{\gamma_2(\gamma_1-1)}{\gamma_1(\gamma_2-1)} \pm \sqrt{\left[(1+\gamma_1 M_{1n}^2)\frac{\gamma_2(\gamma_1-1)}{\gamma_1(\gamma_2-1)}\right]^2 - 4[(\frac{\gamma_1-1}{2}+\frac{\gamma_1-1}{\gamma_2-1})M_{1n}^2(1+\tilde{Q}_d+\frac{\gamma_1-1}{2}M_{1n}^2)]}}{2(\frac{\gamma_1-1}{2}+\frac{\gamma_1-1}{\gamma_2-1})M_{1n}^2}, \tag{5.2}$$

in which γ_1 and γ_2 are the specific heat ratios in the pre- and post-wave states. Based on the above equations, when the incoming flow conditions and heat release are constant, the pressure ratio is constant and the post-wave pressure varies with the incoming pressure. Density acts as a dependent variable (equation 2.15), and therefore varies with pressure.

The incoming velocity is also an important parameter. The post-wave gradient parameters for different incoming Mach numbers are shown in figure 28. An increase in the Mach number significantly affects the post-wave gradients. First, the pressure gradients tend to increase significantly with increasing Mach number. This trend is characterized by a monotonic variation. For the normal velocity, an increase in the Mach number significantly decreases the post-wave gradients and the gradients on either side of $y = 0.9$ change their sign when the Mach number reaches 14. The change in the temperature gradient is similar to that of the pressure gradient. The density gradient generally decreases with increasing Mach number.

As the effect of temperature is not negligible, the post-wave gradient changes with respect to temperature are shown in figure 29. In figure 29, both the post-wave pressure and temperature gradients gradually increase with increasing temperature, whereas both the velocity and density gradients gradually decrease. These changes indicate that the pre-wave temperature significantly affects the post-wave gradient parameters. Temperature affects the local speed of sound, which in turn affects the pre-wave Mach number. In addition, the chemical reaction equation 2.10 implies that temperature significantly affects the process of the chemical reaction, which in turn affects several post-wave parameters. The effect of temperature on the gradient is multifaceted and the mechanism of influence is relatively complex.

Energy release is another important detonation parameter, and different levels of energy

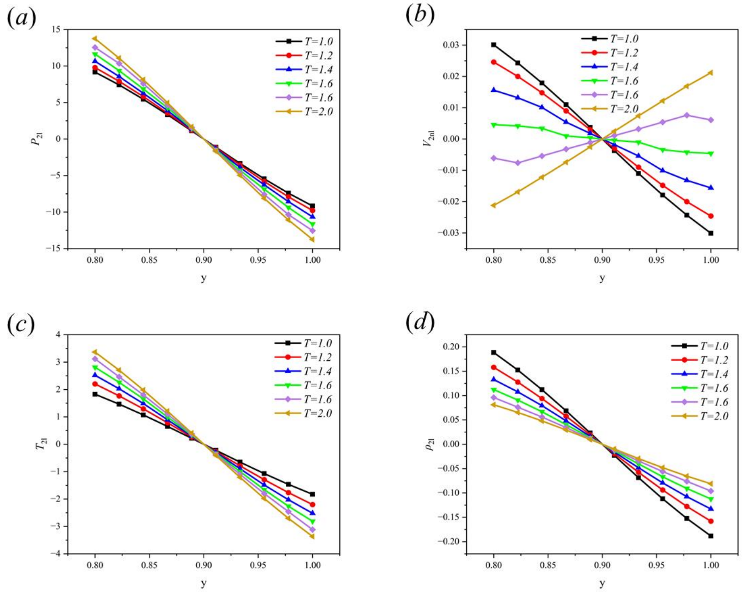

Figure 29: Post-wave gradients for different incoming temperatures: (*a*) pressure, (*b*) velocity, (*c*) temperature, and (*d*) density.

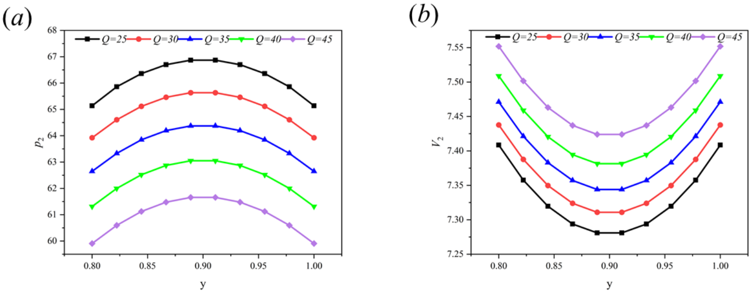

Figure 30: Zero-order parameters for different levels of energy release.

release will have a significant influence on the post-wave parameters. To investigate the effect of energy release on the post-wave first-order gradients, the post-wave pressure and velocity gradients are calculated under different energy releases. Considering that the energy release directly affects post-wave zero-order parameters such as pressure, temperature, velocity, and density, it is first necessary to analyse the variations in the zero-order parameters. In figure 30, the post-wave pressure decreases monotonically and the velocity increases with increasing energy release. The reasons for these change trends can be identified from equations (5.1) and (5.2). In figure 31, the absolute value of the pressure gradient along the m-direction decreases with increasing energy release, which means that the pressure drop is smaller when more energy is released. Similarly, in the y-direction, the absolute value of the pressure gradient along the m-direction decreases with increasing energy release. In figure 32, the normal velocity gradient increases with energy release in both directions, which is the opposite of the pattern for the pressure gradient.

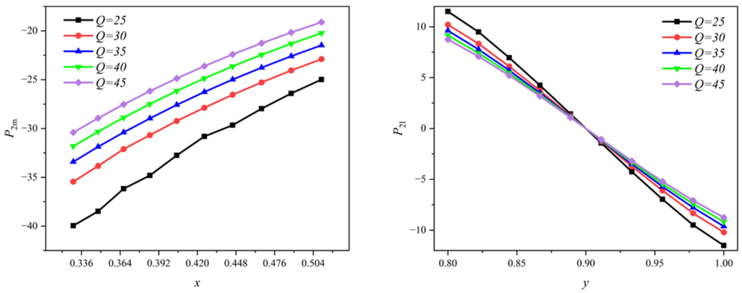

Figure 31: Pressure gradient along xy-plane for different levels of energy release.

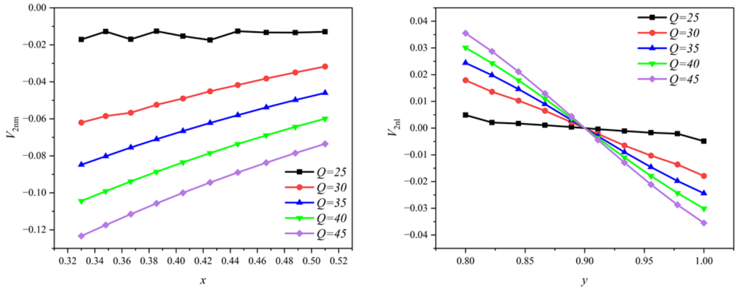

Figure 32: Normal velocity gradient along xy-plane for different levels of energy release.

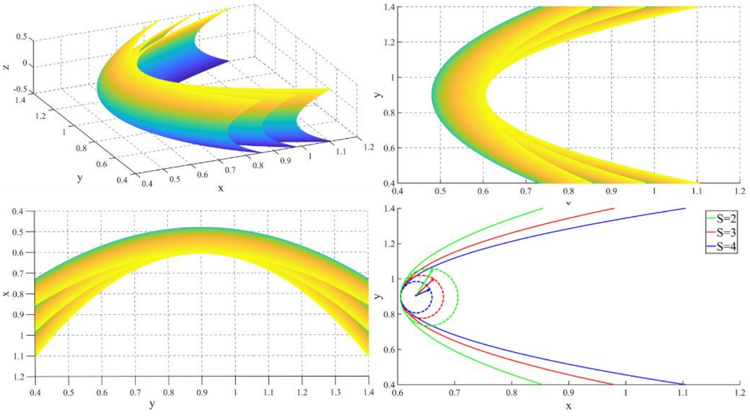

Figure 33: Parabolic wave function of different curvatures.

5.2. *Effect of curvature on post-wave gradients*

The effect of the curvature cannot be ignored in 3D curved detonations. To investigate the effect of the curvature on the post-wave gradients, the calculations in this section consider different curvatures. The geometry is represented by the parabolic function

$$x = S(y + y_0)^2 + x_0, y \in [0.8\ 1], \tag{5.3}$$

where S is used to control the curvature and changing x_0 and y_0 produces translation operations on the x- and y-axes, respectively. This function allows us to obtain detonation waves with different curvatures, as shown in figure 33. Parabolic wave functions with different

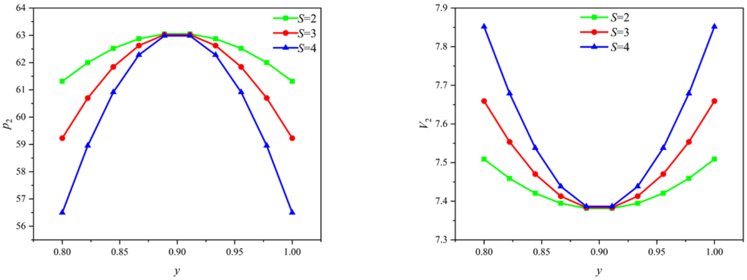

Figure 34: Post-wave pressures and velocities of detonations with different curvatures along the y-direction.

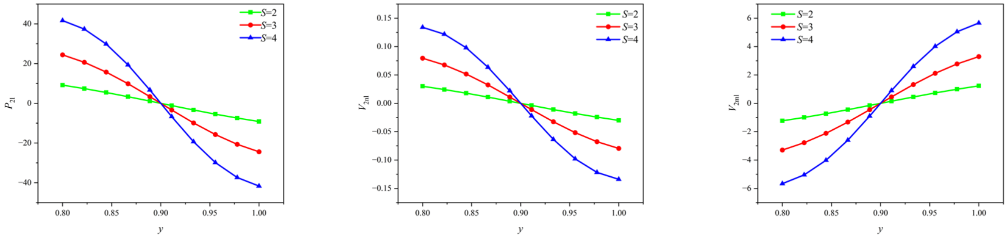

Figure 35: Post-wave pressure and velocity gradients along the y-direction.

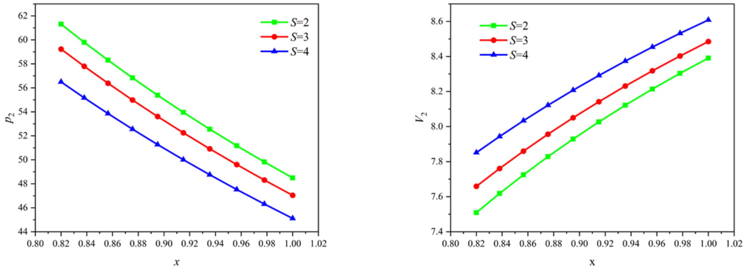

Figure 36: Post-wave pressures and velocities of detonations with different curvatures along the x-direction.

curvatures can be regarded as projectiles with different radii. The corresponding post-wave pressure and velocity and other zero-order parameters are shown in figure 34. The first-order gradients are presented in figure 35. In figure 34, the post-wave pressure peaks at the stationary point and has almost exactly the same value at the peak for different curvatures. This is because, at the stationary point, the wave angles for the different curvatures are almost identical, as can be seen from the geometry. As the curvature S increases, the pressure difference from the stationary point to the two sides gradually increases. The fundamental reason for this phenomenon is that the wave angle changes at a different rate, which results in different pressure gradients along the y-direction, as shown in figure 35. The pressure gradient at the stationary point is zero. To the left of the stationary point, the pressure gradient gradually increases with increasing curvature. The accumulation of the pressure gradient is manifested by the pressure difference from the stationary point to the sides. In contrast to the pressure, the velocity takes a minimal value at the stationary point. First, the normal velocity gradient changes similarly to the pressure gradient, although the magnitude

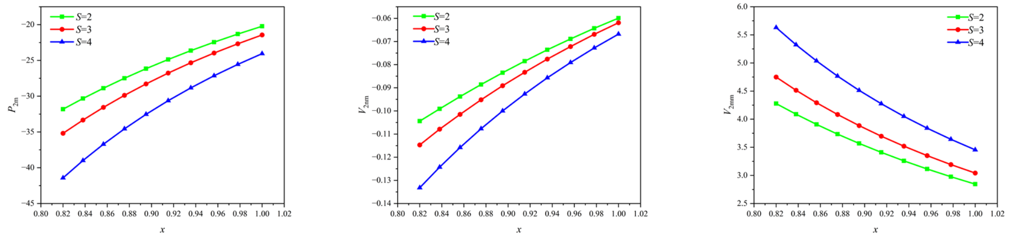

Figure 37: Post-wave pressure and velocity gradients in the x-direction.

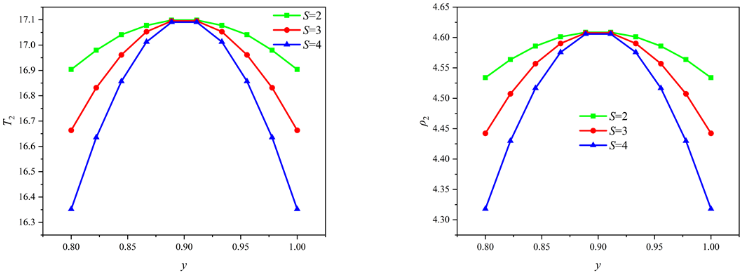

Figure 38: Post-wave temperatures and densities of detonations with different curvatures along the y-direction.

is smaller. Second, the tangential velocity gradient exhibits the opposite change, with the velocity gradient being negative to the left of the stationary point, which indicates that the velocity changes from high to low. On the right of the stationary point, the velocity gradient is positive, suggesting that the velocity changes from low to high.

The zero-order parameters and first-order gradients in the x-direction are also affected by the curvature. As shown in figure 36, the pressure gradually decreases along the x-direction, while the corresponding pressure gradient remains negative. The velocity gradually increases along the x-direction, and the normal (tangential) velocity gradient is always negative (positive). For both temperature and velocity, the pattern is similar to that of the pressure, and will not be repeated.

In real cases, 3D detonation waves may have more complicated shapes, as shown in figures 40(a) and 40(b). Here, the detonation wave curvature changes positively and negatively. To study the gradients under such wave shapes, the variable curvature shown in figure 40(c) is selected, and the two curvatures are named S_1 and S_2, respectively. The post-wave zero-order parameters are plotted in figure 41 along the x-, y-, and z-directions. In figure 41, the variation rules of the zero-order parameters are similar in the x- and z-directions. For example, the wave angle decreases gradually in the x-direction before point o. Therefore, the pressure and temperature decrease, while the velocity increases. After point o, the wave angle increases gradually with increasing x. Thus, the pressure and temperature increase, while the velocity decreases. In the y-direction, with the positive curvature S_1, the x-coordinate at the symmetry point is smaller than on either side. At this time, the wave angle is decreasing with increasing x, so the wave angle is largest at the symmetry point. For the negative curvature S_2, the x-coordinate at the symmetry point is larger than on either side, but here the wave angle is increasing with increasing x, so the wave angle still attains a maximum at the symmetry point. Hence, the zero-order parameters of both curvatures along the y-direction obtain their extreme values at the symmetry point.

After analysing the variations in the zero-order parameters, the first-order gradients are

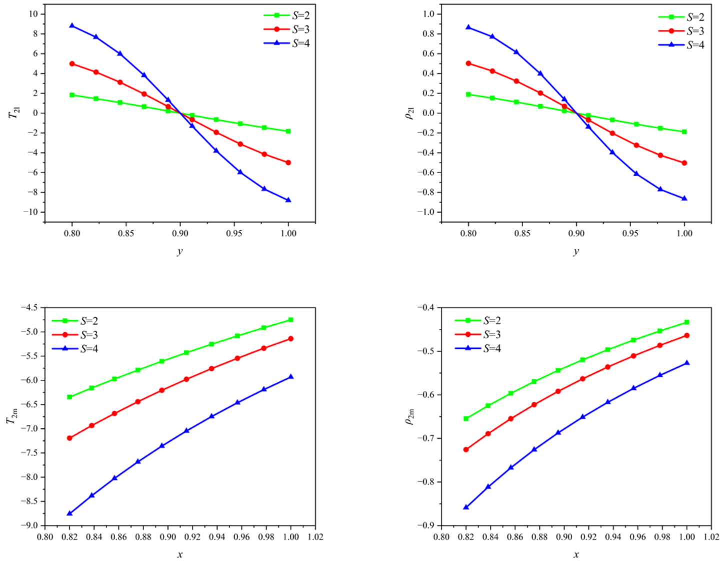

Figure 39: Post-wave temperature and density gradients of detonations with different curvatures along x- and y-directions.

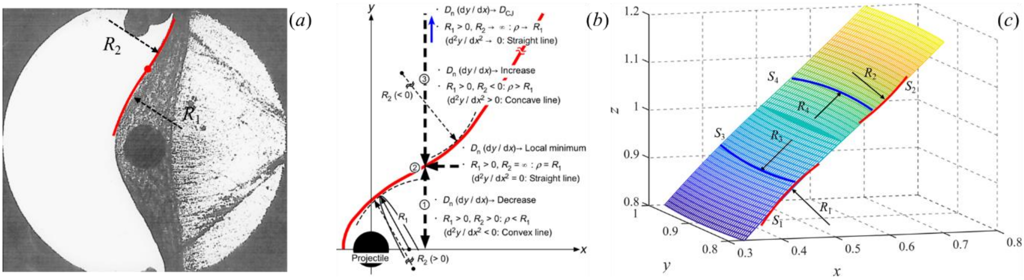

Figure 40: Three-dimensional curved detonation waves with positive and negative curvatures: (a) experimental results of Kaneshige & Shepherd (2002), (b) experimental results of Maeda *et al.* (2013), and (c) stereo view of 3D curved detonation.

now investigated. As shown in figure 42, from the data on the x-edge, the pressure gradient in the l-direction decreases and then increases with increasing x, and turns at point o. However, the pressure gradient along the m-direction is negative in the case of positive curvature and positive in the case of negative curvature. The tangential velocity exhibits similar variations to pressure, except that the gradient changes positively or negatively in both directions. The tangential velocity gradient along the l-direction is negative for both curvatures, but the monotonicity changes at point o. The gradient along the m-direction is positive for S_1 and negative for S_2. The gradient of temperature in the l-direction is similar to that of pressure, but the magnitude is smaller.

The gradients along the y-direction are now discussed. In figure 43(a), the gradient of pressure along the l-direction turns from positive to negative, which means that the maximum value in the l-direction occurs at the stationary point. The magnitude of the gradient is larger for S_1 than for S_2, which is linearly related to the rate of change in the wave angle in both directions. In the m-direction, the pressure gradient on S_1 is negative and reaches a very

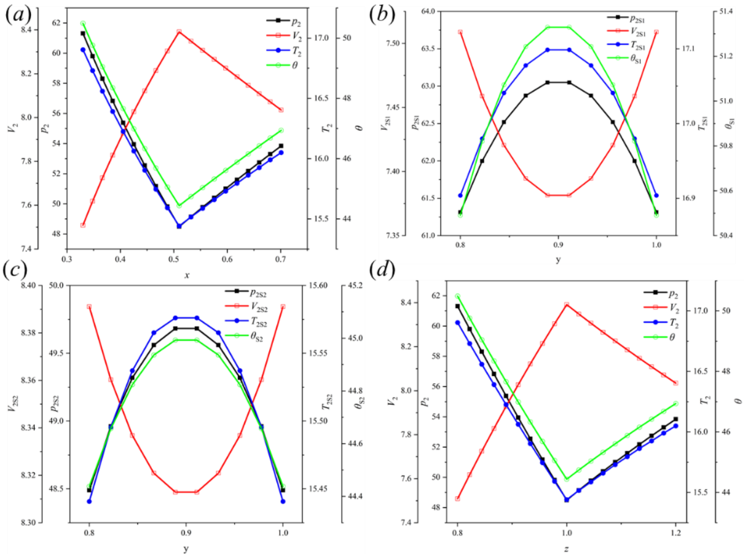

Figure 41: Post-wave zero-order parameters of 3D curved detonation waves with two kinds of curvature: (*a*) variation of zero-order parameters along the *x*-direction, (*b*) variation of zero-order parameters along the S_1-direction in *y*, (*c*) variation of zero-order parameters along the S_2-direction in *y*, and (*d*) variation of zero-order parameters along the *z*-direction.

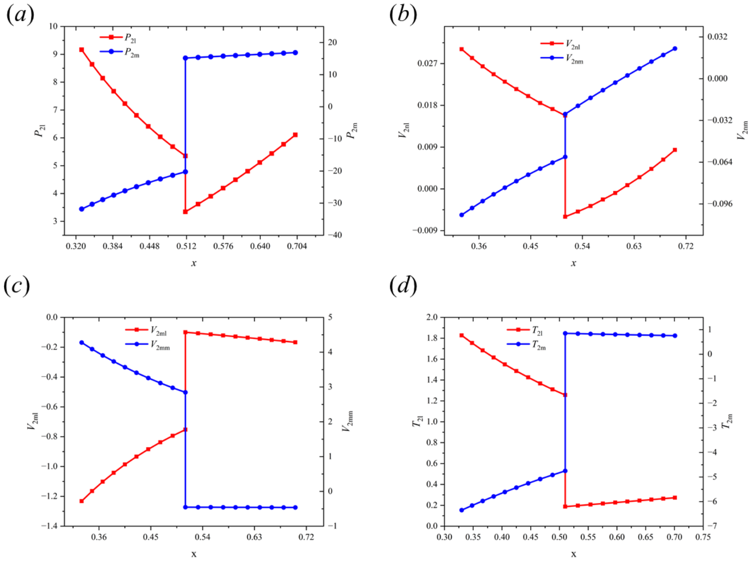

Figure 42: Post-wave first-order gradients of 3D curved detonation waves with two curvatures: (*a*) pressure gradient along the *x*-direction, (*b*) normal velocity gradient along S_1 in the *x*-direction, (*c*) tangential velocity gradient along S_2 in the *x*-direction, and (*d*) temperature gradient along the *x*-direction.

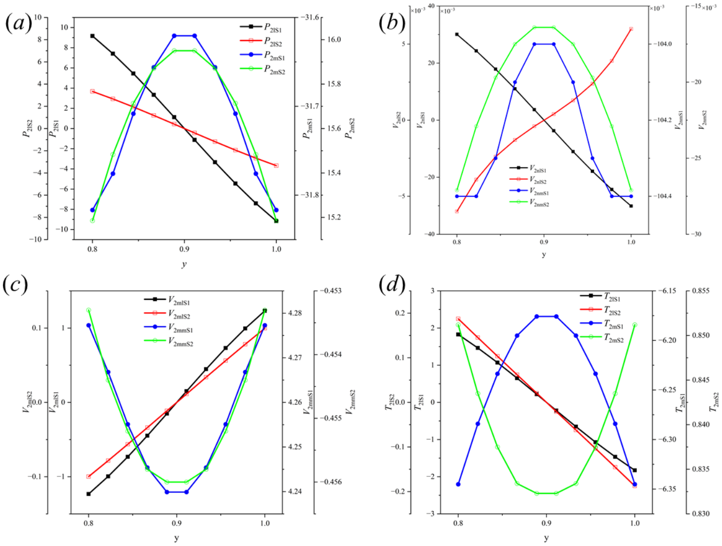

Figure 43: Post-wave first-order gradients of 3D curved detonation waves with two curvatures: (*a*) pressure gradient along the y-direction, (*b*) normal velocity gradient along S_1 in the y-direction, (*c*) tangential velocity gradient along S_2 in the y-direction, and (*d*) temperature gradient along y-direction.

small (absolute) value at the stationary point; the pressure gradient on S_2 is positive and reaches a very large (absolute) value at the stationary point. This is because the curvature in the y-direction has opposite signs. In figure 43(*b*), the gradient of the normal velocity along the l-direction changes from positive to negative on S_1, meaning that the normal velocity increases and then decreases, reaching a maximum value at the stationary point. On S_2, the normal velocity gradient changes from negative to positive, implying that the normal velocity decreases and then increases and reaches a minimum value at the stationary point. The gradient of normal velocity along the m-direction is consistently negative, with the smallest absolute value occurring at the stationary point. In figure 43(*c*), the tangential velocity gradient along the l-direction turns from negative to positive for both curvatures, suggesting that the velocity reaches a minimum value at the stationary point.

5.3. *Verification and inverse solution based on gradients*

To verify the correctness of the proposed 3D curved detonation equations, we now compare the theoretically calculated post-wave gradients with the simulation results, as shown in figure 44. After extracting the post-wave pressure gradients along the x-direction, the pressure gradients along the tangential direction are calculated according to the geometric relationship, as shown by the blue dots. The post-wave gradients can also be calculated using the 3D curved detonation equations, as shown by the red line. The incoming flow parameters are

$$p_1 = 0.421\text{atm}, T_1 = 298K, M_1 = 6.46, R_1 = 397, Q_0 = 2.8 \times 10^6 J/kg, \gamma_1 = 1.40. \qquad (5.4)$$

The corresponding post-wave gradients can be calculated from the 3D curved detonation equations with the fitted wave function. The comparisons show that the error between the theoretical results and the simulation results is relatively small. This indicates that the 3D curved detonation equations proposed in this paper provide a credible means of calculating the post-wave gradients.

The above analysis and application are focused on solving the post-wave gradients for a

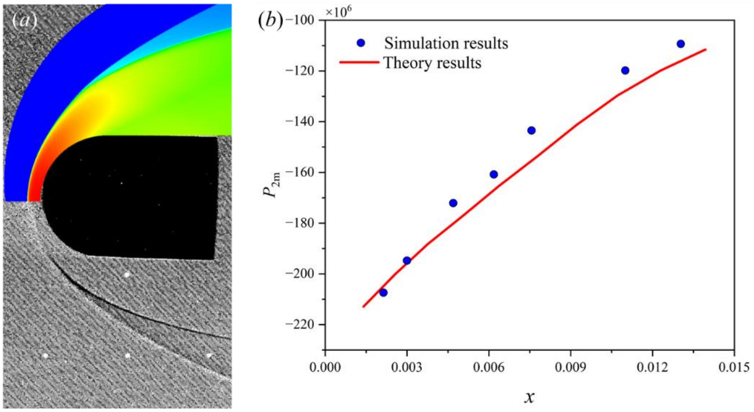

Figure 44: Post-wave gradients extracted from simulation results: (*a*) comparison of the simulation results with the experimental results of Lehr (1972) and (*b*) comparison of post-wave gradients calculated by theory and simulations.

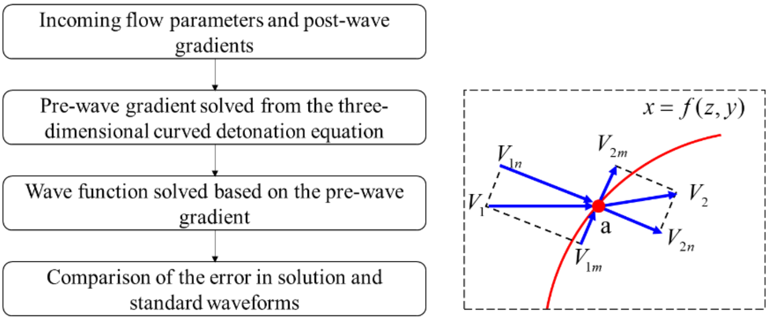

Figure 45: Flowchart for solution of wave function using 3D curved detonation equations.

known wave shape function, which has been verified. In addition to forward solutions, the wave shape function can be obtained from the post-wave gradients via an inverse solution using the 3D curved detonation equations. A flowchart of the specific approach is shown in figure 45. First, the incoming conditions and the post-wave gradients are given. Second, the pre-wave gradients are solved using the 3D curved detonation equations. Third, the wave shape function is determined according to the pre-wave gradients. Finally, the error is computed. If the wave function is written in the general form:

$$F(x, y, z) = a_{11}x^2+a_{22}y^2+a_{33}z^2+2a_{12}xy+2a_{13}xz+2a_{23}yz+2a_{14}x+2a_{24}y+2a_{34}z+a_{44}, \quad (5.5)$$

then the gradient along each of the three directions x, y, z at any point on the wave is:

$$\frac{\partial F}{\partial x} = 2(a_{11}x+a_{12}y+a_{13}z+a_{14}), \frac{\partial F}{\partial y} = 2(a_{12}x+a_{22}y+a_{23}z+a_{24}), \frac{\partial F}{\partial z} = 2(a_{13}x+a_{23}y+a_{33}z+a_{34}). \quad (5.6)$$

The direction vector at that point is:

$$\overrightarrow{n} = \left[\frac{\partial F}{\partial x}, \frac{\partial F}{\partial y}, \frac{\partial F}{\partial z}\right]. \quad (5.7)$$

The velocity vectors are represented as shown in equation (2.1), and the pre-wave velocity gradient in the l-, m-, n-directions can be solved according to the geometric relationship.

	U_{2m}	W_{2m}	U_{1m}	W_{1m}	A	B
(y,z)=(1,1)	0.752	2.845	0.752	2.845	0.5	0.899

Table 1: Solving the wave function at the point (y,z)=(1,1) using the tangential velocity gradient.

	U_{2n}	W_{2n}	U_{1n}	W_{1n}	A	B
(y,z)=(1,1)	-0.0158	-0.0598	-0.767	-2.901	0.499	0.9

Table 2: Solving the wave function at the point (y,z)=(1,1) using the normal velocity gradient.

	U_{2m}	W_{2m}	U_{1m}	W_{1m}	A	B
(y,z)=(0.8,1)	-0.752	2.845	-0.752	2.845	0.499	0.899

Table 3: Solving the wave function at the point (y,z)=(0.8,1) using the tangential velocity gradient.

Using the 3D curved detonation equations, the pre-wave gradients can be determined from the given post-wave gradients. The geometric relationship can be derived from equation (5.8), allowing the wave shape function to be obtained.

$$\begin{cases} U_{1m} = f_1(F), \\ W_{1m} = f_2(F), \\ U_{1n} = f_3(F), \\ W_{1n} = f_4(F). \end{cases} \tag{5.8}$$

To verify this inverse solution method, the function shown in equation (3.18) is used as an example. The incoming flow conditions remain unchanged from equation (3.15). If the shape function of the detonation wave is assumed to be:

$$x = Az^2 + (y - B)^2, \tag{5.9}$$

then there are two unknowns, and it is sufficient to choose two gradients to build the equation:

$$\begin{cases} U_{1m} = f_1(A, B), \\ W_{1m} = f_2(A, B), \end{cases} \text{or} \begin{cases} U_{1n} = f_3(A, B), \\ W_{1n} = f_4(A, B). \end{cases} \tag{5.10}$$

Solving the above equation gives the specific values of the coefficients A, B, from which we can determine the shape function of the detonation wave. If the coordinates $(y, z) = (1, 1)$ and the tangential velocity gradient are selected in equation (5.10), the gradients and coefficients A, B are as listed in table 1. A graphic comparison is presented in figure 46. Similarly, if the normal velocity gradient is selected, the corresponding results are as listed in table 2. A comparison of the data in these tables with the given wave function ($x = 0.5z^2 + (y - 0.9)^2$) clearly demonstrates that the errors in A (compared to 0.5) and B (compared to 0.9) in the inverse solution are very small. The coordinates $(y, z) = (0.8, 1)$ can also be used for verification. The corresponding results are listed in tables 3 and 4. These calculations results verify that the inverse solution method is effective.

The inverse design method can also be applied to 2D curved detonation. Taking the

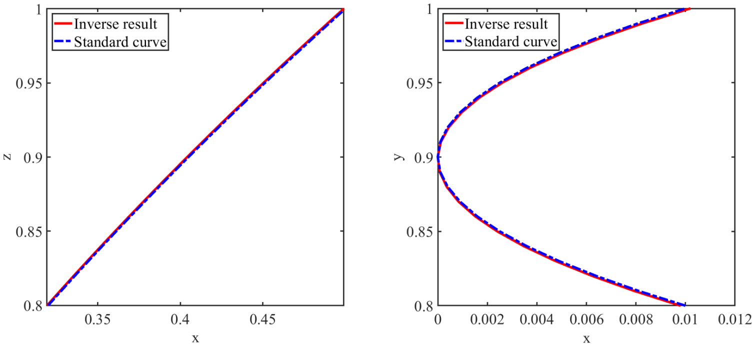

Figure 46: Comparison of the inverse calculation results with the standard curve.

	U_{2n}	W_{2n}	U_{1n}	W_{1n}	A	B
(y,z)=(0.8,1)	0.0158	-0.0598	0.767	-2.901	0.499	0.899

Table 4: Solving the wave function at the point (y,z)=(0.8,1) using the normal velocity gradient.

	U_{2m}	W_{2m}	U_{1m}	W_{1m}	A	B
(x,y)=(0.008563,0.012742)	80972	1205	80972	-78606	-41.01	1.66

Table 5: Solving the wave function at the point (x,y)=(0.008563, 0.012742) using the tangential velocity gradient.

simulation results in figure 44 as an example, we assume that the curved detonation wave is:

$$y = Ax^2 + Bx. \tag{5.11}$$

The post-wave gradients of the curved detonation were calculated in the previous section. Based on the post-wave gradients and the incoming flow parameters, the pre-wave gradients and wave function are as listed in table 5. A comparison with the numerical simulation results is presented in figure 47. The two curves are very similar, which demonstrates the effectiveness of the inverse solution method and 3D curved detonation equations.

6. Conclusions and prospects

This paper has derived the 3D curved detonation equations for solving the post-wave gradients of detonation. The equations were extended to 3D curved detonation waves with bi-directional curvature by modelling the chemical reaction process with a single-step Arrhenius formula in 3D vector space coordinates. The zero-order parameter relationships were derived along the two curvature directions, and the 3D curved detonation equations for solving the pre- and post-wave first-order gradients were obtained. Based on these equations, the influence coefficients of the post-wave gradients were further derived, revealing the influence of the pre-wave gradients on the post-wave gradients. The gradients obtained by the 3D curved detonation equations better explain the variations in zero-order parameters, such as the high temperature and pressure at the stationary point. Using the derived 3D curved detonation

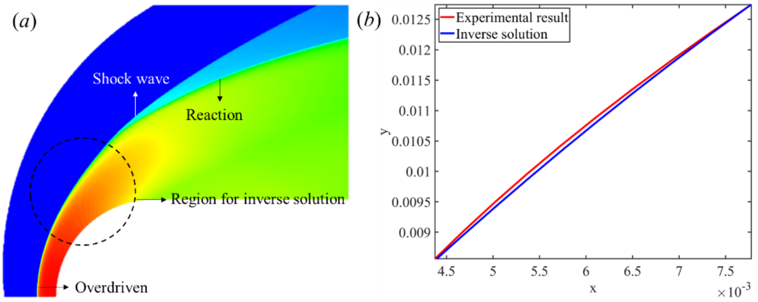

Figure 47: Application of the inverse solution method to planar 2D curved detonation: (a) temperature contour of the simulation results, (b) comparison of the simulation results with the inverse solution.

equations, the root cause of differences in aerodynamic parameters between detonation and shock waves was revealed. Applications based on the equations were developed to further investigate the laws of the incoming flow parameters, energy release, and curvature on the post-wave gradients. The validation of the post-wave gradient parameters and the effectiveness of the inverse solution method demonstrate the effectiveness and superiority of the equations proposed in this paper.

In future work, further derivations will be explored as a means of obtaining the 3D curved detonation equations for second-order gradients. In addition, the single-step Arrhenius equation will be replaced by detailed chemical reaction formulas to further approximate the real chemical reaction process of detonation waves.

Acknowledgements

The authors acknowledge the support of the National Natural Science Foundation of China (Grant Nos. U20A2069, U21B6003, 12472337 and 12302389) and the Advanced Aero-Power Innovation Workstation (Grant No. HKCX2024-01-017).

Declaration of Interests

The authors report no conflict of interest.

Appendix A. Gradients of unit vectors along the three directions

The following describes the derivation of the derivatives of individual unit vectors along multiple directions in a vector coordinate system. A schematic diagram is given in figure 48. In figure 48, for a curve with transversal curvature S_b, the tangent and vertical lines at point O_1 are l_1, n_1, respectively, and the tangent and vertical lines at point O_2 are l_2, n_2, respectively. We consider a Cartesian coordinate system with l_1, n_1 as the x- and y-axis directions and O_1 as the origin. The direction vector along the l_1 curve is $\overrightarrow{e_l}$, and the direction vector along the n_1 curve is $\overrightarrow{e_n}$. From the geometric relationship, we know that the angle between $\overrightarrow{e_l}$ and the x axis is φ. Thus, the vector coordinates are:

$$\overrightarrow{e_l} = (cos\varphi, sin\varphi). \tag{A 1}$$

Correspondingly, the vector coordinates of $\overrightarrow{e_n}$ are:

$$\overrightarrow{e_n} = (sin\varphi, -cos\varphi). \tag{A 2}$$

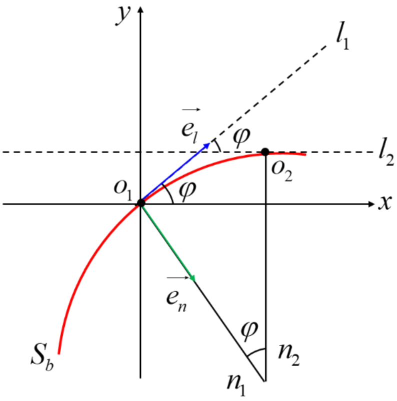

Figure 48: Schematic diagram of 2D axisymmetric direction vectors.

Thus, $\overrightarrow{e_l}$ along φ can be derived as:

$$\frac{\partial \overrightarrow{e_l}}{\partial \varphi} = (-\sin\varphi, \cos\varphi) = -\overrightarrow{e_n}. \tag{A 3}$$

The derivation of $\overrightarrow{e_n}$ along φ yields:

$$\frac{\partial \overrightarrow{e_n}}{\partial \varphi} = (\cos\varphi, \sin\varphi) = \overrightarrow{e_l}. \tag{A 4}$$

Therefore,

$$\frac{\partial \overrightarrow{e_l}}{\partial l} = \frac{\partial \overrightarrow{e_l}}{\partial \varphi}\frac{\partial \varphi}{\partial l} = -\overrightarrow{e_n}S_b, \quad \frac{\partial \overrightarrow{e_n}}{\partial l} = \frac{\partial \overrightarrow{e_n}}{\partial \varphi}\frac{\partial \varphi}{\partial l} = \overrightarrow{e_l}S_b. \tag{A 5}$$

As there is no curvature on the l, m surface, the direction vectors $\overrightarrow{e_m}$ along the l-direction are parallel to one another:

$$\frac{\partial \overrightarrow{e_m}}{\partial l} = 0. \tag{A 6}$$

Similarly, the individual direction vectors along the m-direction can be derived as:

$$\frac{\partial \overrightarrow{e_m}}{\partial m} = \frac{\partial \overrightarrow{e_m}}{\partial \theta}\frac{\partial \theta}{\partial m} = -\overrightarrow{e_n}S_a, \quad \frac{\partial \overrightarrow{e_l}}{\partial m} = 0, \quad \frac{\partial \overrightarrow{e_n}}{\partial m} = \frac{\partial \overrightarrow{e_n}}{\partial \theta}\frac{\partial \theta}{\partial m} = \overrightarrow{e_m}S_a. \tag{A 7}$$

Consider the case in which there is no curvature along the n direction:

$$\frac{\partial \overrightarrow{e_l}}{\partial n} = 0, \quad \frac{\partial \overrightarrow{e_m}}{\partial n} = 0, \quad \frac{\partial \overrightarrow{e_n}}{\partial n} = 0. \tag{A 8}$$

Thus, equation (2.2) has been proved.

Appendix B. Detailed calculation procedure of equation (2.7)

First, calculate the three terms in equation (2.6) separately. The first term is:

$$\begin{aligned}
\overrightarrow{e_l}\frac{\partial(\rho V_l\overrightarrow{e_l}+\rho V_m\overrightarrow{e_m}+\rho V_n\overrightarrow{e_n})}{\partial l} &= \overrightarrow{e_l}[\frac{\partial(\rho V_l\overrightarrow{e_l})}{\partial l}+\frac{\partial(\rho V_m\overrightarrow{e_m})}{\partial l}+\frac{\partial(\rho V_n\overrightarrow{e_n})}{\partial l}] \\
&= \overrightarrow{e_l}[\frac{\partial \rho}{\partial l}V_l\overrightarrow{e_l}+\frac{\partial V_l}{\partial l}\rho\overrightarrow{e_l}+\frac{\partial \overrightarrow{e_l}}{\partial l}\rho V_l+\frac{\partial \rho}{\partial l}V_m\overrightarrow{e_m}+\frac{\partial V_m}{\partial l}\rho\overrightarrow{e_m}+\frac{\partial \overrightarrow{e_m}}{\partial l}\rho V_m+\frac{\partial \rho}{\partial l}V_n\overrightarrow{e_n}+\frac{\partial V_n}{\partial l}\rho\overrightarrow{e_n}+\frac{\partial \overrightarrow{e_n}}{\partial l}\rho V_n] \\
&= \overrightarrow{e_l}[0+0-\overrightarrow{e_n}S_b\rho V_l+\frac{\partial \rho}{\partial l}V_m\overrightarrow{e_m}+\frac{\partial V_m}{\partial l}\rho\overrightarrow{e_m}+0+\frac{\partial \rho}{\partial l}V_n\overrightarrow{e_n}+\frac{\partial V_n}{\partial l}\rho\overrightarrow{e_n}+\overrightarrow{e_l}S_b\rho V_n] \\
&= S_b\rho V_n.
\end{aligned} \tag{B 1}$$

The second term is:

$$\begin{aligned}
\overrightarrow{e_m}\frac{\partial(\rho V_l\overrightarrow{e_l}+\rho V_m\overrightarrow{e_m}+\rho V_n\overrightarrow{e_n})}{\partial m} &= \overrightarrow{e_m}[\frac{\partial(\rho V_l\overrightarrow{e_l})}{\partial m}+\frac{\partial(\rho V_m\overrightarrow{e_m})}{\partial m}+\frac{\partial(\rho V_n\overrightarrow{e_n})}{\partial m}] \\
&= \overrightarrow{e_m}[\frac{\partial \rho}{\partial m}V_l\overrightarrow{e_l}+\frac{\partial V_l}{\partial m}\rho\overrightarrow{e_l}+\frac{\partial \overrightarrow{e_l}}{\partial m}\rho V_l+\frac{\partial \rho}{\partial m}V_m\overrightarrow{e_m}+ \\
&\quad \frac{\partial V_m}{\partial m}\rho\overrightarrow{e_m}+\frac{\partial \overrightarrow{e_m}}{\partial m}\rho V_m+\frac{\partial \rho}{\partial m}V_n\overrightarrow{e_n}+\frac{\partial V_n}{\partial m}\rho\overrightarrow{e_n}+\frac{\partial \overrightarrow{e_n}}{\partial m}\rho V_n] \\
&= \overrightarrow{e_m}[\frac{\partial \rho}{\partial m}V_l\overrightarrow{e_l}+\frac{\partial V_l}{\partial m}\rho\overrightarrow{e_l}+0+\frac{\partial \rho}{\partial m}V_m\overrightarrow{e_m}+\frac{\partial V_m}{\partial m}\rho\overrightarrow{e_m}-\overrightarrow{e_n}S_a\rho V_m+\frac{\partial \rho}{\partial m}V_n\overrightarrow{e_n}+\frac{\partial V_n}{\partial m}\rho\overrightarrow{e_n}+\overrightarrow{e_m}S_a\rho V_n] \\
&= \frac{\partial \rho}{\partial m}V_m+\frac{\partial V_m}{\partial m}\rho+S_a\rho V_n.
\end{aligned} \tag{B 2}$$

The third term is:

$$\begin{aligned}
\overrightarrow{e_n}\frac{\partial(\rho V_l\overrightarrow{e_l}+\rho V_m\overrightarrow{e_m}+\rho V_n\overrightarrow{e_n})}{\partial n} &= \overrightarrow{e_n}[\frac{\partial(\rho V_l\overrightarrow{e_l})}{\partial n}+\frac{\partial(\rho V_m\overrightarrow{e_m})}{\partial n}+\frac{\partial(\rho V_n\overrightarrow{e_n})}{\partial n}] \\
&= \overrightarrow{e_n}[\frac{\partial \rho}{\partial n}V_l\overrightarrow{e_l}+\frac{\partial V_l}{\partial n}\rho\overrightarrow{e_l}+\frac{\partial \overrightarrow{e_l}}{\partial n}\rho V_l+\frac{\partial \rho}{\partial n}V_m\overrightarrow{e_m}+ \\
&\quad \frac{\partial V_m}{\partial n}\rho\overrightarrow{e_m}+\frac{\partial \overrightarrow{e_m}}{\partial n}\rho V_m+\frac{\partial \rho}{\partial n}V_n\overrightarrow{e_n}+\frac{\partial V_n}{\partial n}\rho\overrightarrow{e_n}+\frac{\partial \overrightarrow{e_n}}{\partial n}\rho V_n] \\
&= \overrightarrow{e_n}[\frac{\partial \rho}{\partial n}V_l\overrightarrow{e_l}+\frac{\partial V_l}{\partial n}\rho\overrightarrow{e_l}+0+\frac{\partial \rho}{\partial n}V_m\overrightarrow{e_m}+\frac{\partial V_m}{\partial n}\rho\overrightarrow{e_m}+0+\frac{\partial \rho}{\partial n}V_n\overrightarrow{e_n}+\frac{\partial V_n}{\partial n}\rho\overrightarrow{e_n}+0] \\
&= \frac{\partial \rho}{\partial n}V_n+\frac{\partial V_n}{\partial n}\rho.
\end{aligned} \tag{B 3}$$

Combining the above three expressions leads to equation (2.7). For the equation of conservation of momentum (equation 2.8), we first calculate the gradient operator for the pressure as:

$$\nabla p = \overrightarrow{e_l}\frac{\partial p}{\partial l}+\overrightarrow{e_m}\frac{\partial p}{\partial m}+\overrightarrow{e_n}\frac{\partial p}{\partial n}. \tag{B 4}$$

According to the gradient transformation of the velocity, we have that:

$$\begin{aligned}(\overrightarrow{V}\nabla)\overrightarrow{V} &= V_l\frac{\partial\overrightarrow{V}}{\partial l}+V_m\frac{\partial\overrightarrow{V}}{\partial m}+V_n\frac{\partial\overrightarrow{V}}{\partial n}\\ = V_l\frac{\partial(V_l\overrightarrow{e_l}+V_m\overrightarrow{e_m}+V_n\overrightarrow{e_n})}{\partial l} &+ V_m\frac{\partial(V_l\overrightarrow{e_l}+V_m\overrightarrow{e_m}+V_n\overrightarrow{e_n})}{\partial m}+V_n\frac{\partial(V_l\overrightarrow{e_l}+V_m\overrightarrow{e_m}+V_n\overrightarrow{e_n})}{\partial n}\\ &= 0+V_m(\frac{\partial V_l}{\partial m}\overrightarrow{e_l}+0+\frac{\partial V_m}{\partial m}\overrightarrow{e_m}-\overrightarrow{e_n}S_aV_m+\frac{\partial V_n}{\partial m}\overrightarrow{e_n}+\overrightarrow{e_m}S_aV_n)+\\ &\quad V_n(\frac{\partial V_l}{\partial n}\overrightarrow{e_l}+0+\frac{\partial V_m}{\partial n}\overrightarrow{e_m}+0+\frac{\partial V_n}{\partial n}\overrightarrow{e_n}+0)\\ &= V_m(\frac{\partial V_m}{\partial m}\overrightarrow{e_m}-\overrightarrow{e_n}S_aV_m+\frac{\partial V_n}{\partial m}\overrightarrow{e_n}+\overrightarrow{e_m}S_aV_n)+V_n(\frac{\partial V_l}{\partial n}\overrightarrow{e_l}+\frac{\partial V_m}{\partial n}\overrightarrow{e_m}+\frac{\partial V_n}{\partial n}\overrightarrow{e_n}).\end{aligned} \tag{B 5}$$

Organizing the above expressions along each of the three directions leads to equation (2.9):
For the l direction:

$$\rho V_n\frac{\partial V_l}{\partial n}+\frac{\partial p}{\partial l}=0. \tag{B 6}$$

For the m direction:

$$\rho V_m\frac{\partial V_m}{\partial m}+\rho V_n\frac{\partial V_m}{\partial n}+\frac{\partial p}{\partial m}+\rho V_mV_nS_a=0. \tag{B 7}$$

For the n direction:

$$\rho V_m\frac{\partial V_n}{\partial m}+\rho V_n\frac{\partial V_n}{\partial n}+\frac{\partial p}{\partial n}-\rho V_m^2S_a=0. \tag{B 8}$$

Appendix C. Complete derivation of influence coefficient equations

If we set:

$$(C_{21}C_{27}-C_{23}C_{25})=C_{17}^{35},(C_{25}C_{211}-C_{27}C_{29})=C_{511}^{79}, \tag{C 1}$$

then,

$$\begin{gathered}(C_{11}C_{27}-C_{23}C_{15})C_{511}^{79}P_{1l}+((C_{12}-C_{22})C_{27}-(C_{16}-C_{26})C_{23})C_{511}^{79}U_{1m}+(C_{13}C_{27}-\\ C_{23}C_{17})C_{511}^{79}U_{1n}+(C_{14}C_{27}-C_{23}C_{18})C_{511}^{79}K_{1l}=C_{17}^{35}C_{511}^{79}P_{2l}+(C_{24}C_{27}-C_{23}C_{28})C_{511}^{79}K_{2l},\end{gathered} \tag{C 2}$$

and

$$\begin{gathered}(C_{15}C_{211}-C_{27}C_{19})C_{17}^{35}P_{1l}+((C_{16}-C_{26})C_{211}-(C_{110}-C_{210})C_{27})C_{17}^{35}U_{1m}+(C_{17}C_{211}-\\ C_{27}C_{111})C_{17}^{35}U_{1n}+(C_{18}C_{211}-C_{27}C_{112})C_{17}^{35}K_{1l}=C_{17}^{35}C_{511}^{79}P_{2l}+(C_{28}C_{211}-C_{27}C_{212})C_{17}^{35}K_{2l}.\end{gathered} \tag{C 3}$$

Subtracting one equation from the other gives:

$$\begin{gathered}((C_{11}C_{27}-C_{23}C_{15})C_{511}^{79}-(C_{15}C_{211}-C_{27}C_{19})C_{17}^{35})P_{1l}\\ +(((C_{12}-C_{22})C_{27}-(C_{16}-C_{26})C_{23})C_{511}^{79}-((C_{16}-C_{26})C_{211}-(C_{110}-C_{210})C_{27})C_{17}^{35})U_{1m}\\ +((C_{13}C_{27}-C_{23}C_{17})C_{511}^{79}-(C_{17}C_{211}-C_{27}C_{111})C_{17}^{35})U_{1n}+((C_{14}C_{27}-C_{23}C_{18})C_{511}^{79}-(C_{18}C_{211}-\\ C_{27}C_{112})C_{17}^{35})K_{1l}=((C_{24}C_{27}-C_{23}C_{28})C_{511}^{79}-(C_{28}C_{211}-C_{27}C_{212})C_{17}^{35})K_{2l}.\end{gathered} \tag{C 4}$$

Then, we can write:

$$\begin{gathered}
K_{2l} = ((C_{11}C_{27} - C_{23}C_{15})C_{511}^{79} - (C_{15}C_{211} - C_{27}C_{19})C_{17}^{35})/((C_{24}C_{27} - C_{23}C_{28})C_{511}^{79} - \\
(C_{28}C_{211} - C_{27}C_{212})C_{17}^{35})P_{1l} + (((C_{12} - C_{22})C_{27} - (C_{16} - C_{26})C_{23})C_{511}^{79} - ((C_{16} - C_{26})C_{211} - \\
(C_{110} - C_{210})C_{27})C_{17}^{35})/((C_{24}C_{27} - C_{23}C_{28})C_{511}^{79} - (C_{28}C_{211} - C_{27}C_{212})C_{17}^{35})U_{1m} + ((C_{13}C_{27} - \\
C_{23}C_{17})C_{511}^{79} - (C_{17}C_{211} - C_{27}C_{111})C_{17}^{35})/((C_{24}C_{27} - C_{23}C_{28})C_{511}^{79} - (C_{28}C_{211} - C_{27}C_{212})C_{17}^{35})U_{1n} \\
+((C_{14}C_{27} - C_{23}C_{18})C_{511}^{79} - (C_{18}C_{211} - C_{27}C_{112})C_{17}^{35})/((C_{24}C_{27} - C_{23}C_{28})C_{511}^{79} - \\
(C_{28}C_{211} - C_{27}C_{212})C_{17}^{35})K_{1l}.
\end{gathered} \tag{C 5}$$

If we define:

$$\begin{gathered}
J_k = ((C_{11}C_{27} - C_{23}C_{15})C_{511}^{79} - (C_{15}C_{211} - C_{27}C_{19})C_{17}^{35})/((C_{24}C_{27} - C_{23}C_{28})C_{511}^{79} - \\
(C_{28}C_{211} - C_{27}C_{212})C_{17}^{35}), \\
L_k = (((C_{12} - C_{22})C_{27} - (C_{16} - C_{26})C_{23})C_{511}^{79} - ((C_{16} - C_{26})C_{211} - (C_{110} - C_{210})C_{27})C_{17}^{35}) \\
/((C_{24}C_{27} - C_{23}C_{28})C_{511}^{79} - (C_{28}C_{211} - C_{27}C_{212})C_{17}^{35}), \\
I_k = ((C_{13}C_{27} - C_{23}C_{17})C_{511}^{79} - (C_{17}C_{211} - C_{27}C_{111})C_{17}^{35})/((C_{24}C_{27} - C_{23}C_{28})C_{511}^{79} - \\
(C_{28}C_{211} - C_{27}C_{212})C_{17}^{35}), \\
N_k = ((C_{14}C_{27} - C_{23}C_{18})C_{511}^{79} - (C_{18}C_{211} - C_{27}C_{112})C_{17}^{35})/((C_{24}C_{27} - C_{23}C_{28})C_{511}^{79} - \\
(C_{28}C_{211} - C_{27}C_{212})C_{17}^{35}),
\end{gathered} \tag{C 6}$$

then

$$K_{2l} = J_k P_{1l} + L_k U_{1m} + I_k U_{1n} + N_k K_{1l}. \tag{C 7}$$

Combining these two expressions, we obtain:

$$\begin{gathered}
C_{11}P_{1l} + (C_{12} - C_{22})U_{1m} + C_{13}U_{1n} + C_{14}K_{1l} \\
= C_{21}(J_p P_{1l} + L_p U_{1m} + I_p U_{1n} + N_p K_{1l}) + C_{23}U_{2n} + C_{24}(J_k P_{1l} + L_k U_{1m} + I_k U_{1n} + N_k K_{1l}).
\end{gathered} \tag{C 8}$$

Further rearrangement yields:

$$\begin{aligned}
U_{2n} = {} & (C_{11} - C_{21}J_p - C_{24}J_k)/C_{23}P_{1l} + ((C_{12} - C_{22}) - C_{21}L_p - C_{24}L_k)/C_{23}U_{1m} \\
& +(C_{13} - C_{21}I_p - C_{24}I_k)/C_{23}U_{1n} + (C_{14} - C_{21}N_p - C_{24}N_k)/C_{23}K_{1l}.
\end{aligned} \tag{C 9}$$

We define the following notation:

$$\begin{aligned}
J_u &= (C_{11} - C_{21}J_p - C_{24}J_k)/C_{23}, \\
L_u &= ((C_{12} - C_{22}) - C_{21}L_p - C_{24}L_k)/C_{23}, \\
I_u &= (C_{13} - C_{21}I_p - C_{24}I_k)/C_{23}, \\
N_u &= (C_{14} - C_{21}N_p - C_{24}N_k)/C_{23}.
\end{aligned} \tag{C 10}$$

Then,

$$U_{2l} = J_u P_{1l} + L_u U_{1m} + I_u U_{1n} + N_u K_{1l}. \tag{C 11}$$

At this stage, the complete influence coefficient equations are available.

REFERENCES

Agafonov, GL & Frolov, SM 1994 Computation of the detonation limits in gaseous hydrogen-containing mixtures. *Combustion, Explosion and Shock Waves* **30** (1), 91–100.

Choi, J.-Y., Kim, D.-W., Jeung, I.-S., Ma, F. & Yang, V. 2007 Cell-like structure of unstable oblique detonation wave from high-resolution numerical simulation. *Proc. Combust. Inst.* **31** (2), 2473–2480.

Crane, Jackson, Lipkowicz, Jonathan T, Shi, Xian, Wlokas, Irenaeus, Kempf, Andreas M & Wang, Hai 2023 Three-dimensional detonation structure and its response to confinement. *Proceedings of the Combustion Institute* **39** (3), 2915–2923.

Doering, W. 1943 On the detonation process in gases. *Annuals of Physics* **435**, 421–436.

Gato, CH 2010 Detonation-driven fracture in thin shell structures: Numerical studies. *Applied Mathematical Modelling* **34** (12), 3741–3753.

Han, Wenhu, Wang, Cheng & Law, Chung K. 2019 Three-dimensional simulation of oblique detonation waves attached to cone. *Physical Review Fluids* **4** (5).

He, Longting & Lee, John HS 1995 The dynamical limit of one-dimensional detonations. *Physics of Fluids* **7** (5), 1151–1158.

Jiang, Zonglin, Zhang, Zijian, Yunfeng, LIU, Chun, WANG & Changtong, LUO 2021 Criteria for hypersonic airbreathing propulsion and its experimental verification. *Chinese Journal of Aeronautics* **34** (3), 94–104.

Kaneshige, Michael J. & Shepherd, J. E. 2002 Oblique detonation stabilized on a hypervelocity projectile. *Explosion and Shock Waves* **26** (2), 3015–3022.

Lefebvre, MH & Fujiwara, T 1995 Numerical modeling of combustion processes induced by a supersonic conical blunt body. *Combustion and Flame* **100** (1-2), 85–93.

Lehr, H.F. 1972 Experiments on shock-induced combustion. *Astronautica Acta* **17**, 589–597.

Liu, Yan, Han, Xudong, Yao, Songbai & Wang, Jianping 2016 A numerical investigation of the prompt oblique detonation wave sustained by a finite-length wedge. *Shock Waves* **26**, 729–739.

Maeda, Shinichi, Sumiya, Satoshi, Kasahara, Jiro & Matsuo, Akiko 2013 Initiation and sustaining mechanisms of stabilized oblique detonation waves around projectiles. *Proceedings of the Combustion Institute* **34** (2), 1973–1980.

Mölder, S 2016 Curved shock theory. *Shock Waves* **26** (4), 337–353.

von Neumann, John 1942 Theory of detonation waves. *John von Neumann, collected works* **6**, 203–218.

Teng, Honghui, Tian, Cheng, Zhang, Yining, Zhou, Lin & Ng, Hoi Dick 2021 Morphology of oblique detonation waves in a stoichiometric hydrogen–air mixture. *Journal of Fluid Mechanics* **913**, A1.

Teng, H. H. & Jiang, Z. L. 2012 On the transition pattern of the oblique detonation structure. *J. Fluid Mech.* **713**, 659–669.

Verreault, Jimmy. 2012 Initiation of gaseous detonation by conical projectiles. PhD thesis, McGill University (Canada).

Verreault, Jimmy & Higgins, Andrew J 2011 Initiation of detonation by conical projectiles. *Proceedings of the Combustion Institute* **33** (2), 2311–2318.

Viguier, Christophe, Da Silva, Luís Fernando Figueira, Desbordes, Daniel & Deshaies, Bruno 1996 Onset of oblique detonation waves: Comparison between experimental and numerical results for hydrogen-air mixtures. In *Symposium (International) on Combustion*, , vol. 26, pp. 3023–3031. Elsevier.

Wang, Cheng, Lu, J & Ye, T 2008 Numerical simulation of three-dimensional gas detonation. In *Journal of Physics: Conference Series*, , vol. 96, p. 012029. IOP Publishing.

Wolański, Piotr 2013 Detonative propulsion. *Proceedings of the Combustion Institute* .

Yan, Hao, Xiong, Haochen, Han, Xin, Shi, Chongguang & You, Yancheng 2024 A theoretical method for oblique and curved detonation waves. *Physics of Fluids* **36** (6), 066108.

Yang, Pengfei, Ng, Hoi Dick, Teng, Honghui & Jiang, Zonglin 2017 Initiation structure of oblique detonation waves behind conical shocks. *Physics of Fluids* **29** (8).

Yungster, S., Radhakrishnan, K. & Perkins, High D. 2003 Structure and stability of one-dimensional detonations in ethylene-air mixtures. In *33rd AIAA Fluid Dynamics Conference and Exhibit*.

Zel'dovich, Yakov B 1940 On the theory of the propagation of detonation in gaseous systems. *Zh. eksp. teoret. fiz.* **10**, 542–568.